SHALLOW COMPOSITION AND STRUCTURE OF THE UPPER PART OF THE EXHUMED SAN GABRIEL FAULT, CALIFORNIA: IMPLICATIONS FOR FAULT PROCESSES AND SEISMIC PROPERTIES

Kaitlyn Crouch[1,2]
James P. Evans[1.]
Susanne U. Jänecke[1]

[1]Department of Geosciences, 4505 Old Main Hill, Utah State University, Logan, UT. 84322-4505

[2]Now at: Department of Geosciences, Lewis G. Weeks Hall, 1215 West Dayton Street, University of Wisconsin, Madison, WI 53706-1692

This is a pre-submitted preprint of a paper that we intend to submit to Tektonika by November 1, 2022.

Comments and suggestions are welcome.

October 21, 2022

SHALLOW COMPOSITION AND STRUCTURE OF THE UPPER PART OF THE EXHUMED SAN GABRIEL FAULT, CALIFORNIA: IMPLICATIONS FOR FAULT PROCESSES AND SEISMIC PROPERTIES

Kaitlyn Crouch[1,2]
James P. Evans[1.]
Susanne U. Jänecke[1]

[1]Department of Geosciences, 4505 Old Main Hill, Utah State University, Logan, UT. 84322-4505
[2]Now at: Department of Geosciences, Lewis G. Weeks Hall, 1215 West Dayton Street, University of Wisconsin, Madison, WI 53706-1692

ABSTRACT

Analyses of the composition, properties, and structure of the upper parts of fault zones constrain the mechanical and seismological behavior of faults. We examine macro- to microstructures of fault-related rocks across the San Gabriel Fault zone, California, which was active 5-12 mya and exhibits evidence of Quaternary slip. The steeply plunging ALT-B2 geotechnical borehole encountered an upper ~60 m thick damage zone and a 20-m thick lower damage zone, and two principal slip zones composed of cohesive cataclasite, ultracataclasite, and intact clay gouge within them. The upper ~6.5 m thick principal slip zone separates Mendenhall Gneiss and Josephine Granodiorite, and a lower 11-m thick principal slip is enclosed within the Josephine Granodiorite. Microstructures recorded in core and field samples document overprinted brittle fractures, cohesive cataclasites, veins, sheared clay-rich rocks, and folded foliated horizons in the damage zones. Carbonate veins are common in the lower fault zone, and alteration and mineralization assemblages consist of clays, epidote, calcite, zeolites, and chloritic minerals. Highly altered, mineralized, and deformed rocks in the principal slip zones have very low rock mass rating values. This indicates that portions of the fault zones have very low Young's moduli and V_s and V_p values as low as 500 and 1000m/sec, respectively, well below the protolith values recorded in a nearby borehole. These data show syntectonic grain-scale alteration, mineralization, and deformation result in low seismic velocities and weak fault-related rocks in the shallow crust and reduced moduli may impact the distribution of seismic energy and slip to the surface.

1. Introduction

The paucity of data on the composition, microstructures, and properties of fault-related rocks in the shallow parts of fault zones limits our ability to model seismic energy and slip distribution (Nevitt et al., 2020; Marchandon et al., 2021). The shallow parts of faults - which we define here as the top of faulted bedrock to depths of ~ 2-3 km (Figure 1) is a transitional zone where fault slip and energy are distributed from seismogenic depths to the near-surface region (Figure 1; Kaneko and Fialko, 2011; Roten et al., 2017; Marone and Saffer, 2007). The range of dominant deformation mechanisms and fault-related rock composition, typically determined from microstructural, mineralogic, and geochemical studies, indicate that the uppermost regions of faults consist of gouge and breccia, which give way to cataclasites at 2-3 km (Figure 1A). These observations suggest that frictional and thus seismic behavior is dominated by stable sliding and lack of earthquake nucleation. This is borne out by recent analyses of the Southern California earthquake catalog (Haukkson and Meir, 2019; Figure 1B) and from slip inversions for recent large-magnitude earthquakes (Figure 1C). Classic models of fault deformation and fault-related rocks as a function of depth (Figure 1; Scholz, 1988; 2019; Sibson, 1977; Woodcock and Mort, 2008), define the shallow fault-related rock in the upper ~2-3 km as comprising of clay gouge, fault breccias, and/or incohesive fault-related rocks. However, the composition and structure of active faults may consist of cohesive, altered, and highly sheared rocks (Boulton et al., 2017) and thin fault cores within damage zones comprised of complexly deformed and altered rocks (Chester and Logan, 1986; Chester et al., 1993; Mitchell and Faulkner, 2009). These aspects of fault zone structure and composition indicate that fault zones may experience considerably more complex behavior than previous models suggest (Figure 1A).

Continuous drill core and related data acquired in a geotechnical investigation through the San Gabriel Fault, California (SGF) (Figure 2), allow access to fault-related rocks that formed at ~2-3 km deep. The drill holes provide access to unweathered rocks in core and borehole-based geophysical data. We integrate macro- to microscale analyses of the drill core with analyses of outcrop samples and rock mechanics-based data to determine the deformation mechanisms, alteration, and physical and mineralogic properties of fault-related rocks within the upper fault zone. Rock quality data are used to estimate the elastic properties of the fault zone, and relate the geologic characterization of the fault-related rocks to estimates of elastic moduli. This provides critical data for models of the response of the shallow parts of faults to seismic slip at depth (Roten et al., 2017a; Nevitt et al., 2020).

1.1 Geologic Setting

The San Gabriel Fault (SGF) in the San Gabriel Mountains, California, (Figure 2) accommodated >40 km of right-lateral slip between 12 to 5 million years ago (Powell et al., 1993; Nourse, 2002) in the early development of the San Andreas fault system. The fault has since been uplifted and exhumed due to slip on the underlying north-dipping Sierra Madre thrust fault. We sampled these rocks that are interpreted to have formed at 2-2.5 km depth in the SGF (Bull, 1978; Chester et al., 1993; Blythe et al., 2002). The majority of the deformation recorded in the fault-related rocks occurred at depth during the most active phase of the SGF (Citation?). Quaternary slip rates of 0.2 to 1 mm/yr estimated for the southern strand of the SGF are ~8-10 times slower than its most active rate in the Mio-Pliocene (Weber,1982; Yeats et al., 1994; Lee and Schwarcz, 1996). Evidence for Quaternary slip in the form of aligned canyons, offset Miocene-Pliocene deposits, and the presence of possible degraded fault scarps (Beyer et al., 2009) indicate that as much as 5 km of post-Miocene slip is possible along parts of the San Gabriel and Vasquez faults (Beyer et al., 2009; Bryant, 2017). Anderson et al. (1983), Chester et al., (1993), and Evans and Chester (1995) examined surface expressions of the SGF to the southeast of the drill site. Chester et al. (1993) examined rocks exhumed from depths of at least 3.5 km (Blythe et al., 2002), and the sites studied in Anderson et al. (1983) and field outcrop samples in this work were exhumed ~ 2 km in the Tujunga fault block (Blythe et al., 2002).

The San Gabriel Mountains are composed of medium- to coarse-grained Precambrian and Cretaceous gneiss, granite, granodiorite, amphibolite, and gabbro of the Mendenhall Gneiss and Mt. Lowe Intrusive Suite (Figure 2; Barth and Ehlig, 1988; Anderson et al., 1983; Campbell et al., 2014). Multiple traces of the SGF are mapped along the fault zone and are up to ~100 m apart (Jennings and Strand; 1969; Dibblee and Ehrenspeck, 1991; Dibblee and Carter, 2002; Yerkes et al., 2005; Campbell et al., 2014). In the central San Gabriel Mountains, the SGF splits into the north and south branches, with the south branch joining the Sierra Madre-Cucamonga thrust system to the southeast. Slip along the surface trace of the SGF is confined to a principal slip zone consisting of cm- to m-thick zones of ultracataclasite and foliated cataclasite (Anderson et al., 1983; Chester et al., 1993; Evans and Chester, 1995). We use drill core acquired across the SGF and field samples from the surface expression of the SGF in the Little and Big Tujunga Canyons that formed at depths of 2-2.5 km (Blythe et al., 2002) in the SGF.

1.1.1. ALT-B2 Geotechnical Core

The California High-Speed Rail Authority (CHSRA) collected drill core in 2016 from the ALT-B2 borehole as part of a geotechnical survey across the SGF at depth (Figures 2B, 3). At the ALT-B2 borehole site, the steep north-dipping fault juxtaposes Precambrian Mendenhall Gneiss on the north side against Cretaceous leucocratic granitic rocks interlayered with Cretaceous (?) quartz diorite (Dibblee and Eherenspeck, 1991; Figures 2 and 3). The ALT-B2 borehole was drilled with a plunge of ~68° to 162°, reaching a total drill hole depth (TD) of 493.1 m and a true vertical depth of 457.2 m. This formed a ~32° angle with the ~80° north-dipping SGF (Figure 3), and the borehole samples an extensive portion of the fault damage zone and principal slip zones. The north dip of the fault is determined by connecting the mapped surface trace near the drill site to the shallowest fault core encountered in the fault zone, and from field data for the dip of the fault nearest the drill site (see below).

The ALT-B2 borehole was drilled using an HQ drill rod with an 8.9 cm diameter coring system and spudded at 34.359514°N, 118.398809°W (371364.94E, 3802894.69N, UTM zone 115) at an elevation of 864.38 m above sea level (2,835.89 ft). Poor borehole conditions in the fault zone region of ALT-B2 through the SGF resulted in difficult drilling conditions and “clay-squeezing” in parts of the borehole and a lack of borehole-based seismic velocity measurements. Geotechnical reports (CHSRA, 2019) provide data on lithology, rock quality designation (RQD), hardness, weathering, fracture density, unadjusted rock mass rating (RMR), geological strength index (GSI), and rock mass quality (Q) of nearly 493 m of core (Supplemental Files 1,2 and 8). The drill core was sampled at field storage facilities in 2018 and 2019.

1.1.2. Little and Big Tujunga Canyon Exposures

Field exposures of the San Gabriel Fault ~ 4 to 20 km southeast of the ALT-B2 drill site (Figure 2) in Little Tujunga and Big Tujunga canyons provide further insights and samples from the fault zone (see Anderson et al., 1983). The main trace of the SGF in Little Tujunga Canyon (sites LT1 and LT2) juxtaposes Mendenhall Gneiss and Josephine Granodiorite, with a small outcrop of Tertiary siltstone and mudstones of the Santa Susanna Formation (?) in the fault zone (Dibblee and Eherenspeck, 1991) at LT1. Big Tujunga sites BT1 and BT2 are ~16 km east-southeast of the drill site, and here the fault consists of two strands. North of the northern strand, the rocks consist of Cretaceous quartz diorite. Rocks between the faults are highly fractured gneiss and Cretaceous granitic rocks. The SGF splits into north and south branches at ~ 19 km south-southeast of the drill site, and site BT4 provides exposures of fault-related rocks in a series of 4 faults of the North Branch of the San Gabriel Fault. The rocks north of the Maple Canyon strand of the fault zone are leucocratic Cretaceous granitic rocks, with a ~ 250 m wide zone of faulted and altered rocks in the fault zone and quartz monzonites south of the zone (Dibblee and Carter, 2002). The SGF manifests at these sites as thin ultracataclasite zones, gouge zones, and zones of brecciation and damage (Anderson et al., 1983; J. S. Caine, pers. comm., 2021; d'Alessio, 2004). These fault-related rocks formed at depths of ~2 km and were later exhumed to the surface (Blythe et al., 2002).

2. Methods

We document the physical and chemical properties of fault-related rocks and examine the evidence for deformation, fluid-rock interaction, and changes in mineralogy within the upper seismic-aseismic transition zone of the SGF. We integrate macroscopic drill core and outcrop sample analyses, optical microscopy, and X-ray diffraction mineralogic analyses, and link these results with borehole-based measurements of fracture densities and rock mass rating data to determine the fault zone structure, deformation mechanisms, and alteration patterns. Here we focus on the macroscopic and microstructural nature of the deformed rocks from drill core samples. We supplement drill core data with data from outcrop samples from the Little and Big Tujunga canyons (J. S. Caine, pers. comm, 2021). The ALT-B2 drill core dataset includes borehole data provided by California High-Speed Rail Authority (2019), 28 core samples, 28 thin sections, and 34 X-ray diffraction (XRD) measurements (Supplemental Files). The field sample dataset consists of 26 field samples and 34 thin sections.

Mesoscopic analyses of the drill core document the lithologies, shear fabrics, nature of the alteration, the intensity of deformation, and the distribution of veins, slip surfaces, and other indicators of fluid-rock interactions. The ALT-B2 borehole samples a large portion of the fault damage zone, with an average drill core recovery rate of 95%. Samples we examined in detail consist of 5.12 m of drill core from 28 sites along the core (Figure 3; Table 1). Drill core samples were chosen using on-site geologists' notes and geotechnical core log data to encompass the entirety of the length of the drill core and to target protolith and fault-related rocks within the principal slip zones and damage zones. We compiled the fracture density data and the geotechnical rock mass rating from the geotechnical data to determine the physical properties of the cored rocks. Drill core samples are typically very well-indurated and we applied epoxy to the outer surfaces as a precaution to preserve the integrity of the core and structures.

The conditions and nature of the cored rock were compiled by the project geologists, and we used some of these data on the 493 m of the core to quantify the mechanical properties of the fault-related rocks and to calculate their sonic velocities. Observations of the core are reported as RQD values (see Supplemental files 2 and 8 for details), and from these data, values of RMR_{1989} are determined. The RMR_{1989} values (Figure 3) quantify rock strength for its engineering stability (Bieniawski, 1989; Zhang, 2016) and are combinations of six parameters (see Supplemental File 8): uniaxial compressive strength (UCS) of intact rock, rock quality designation (RQD), joint or discontinuity spacing, joint or rock fracture conditions, groundwater conditions, and joint orientation (Bieniawski, 1978; 1989; Singh and Goel, 2011)). RMR_{1989} values of 0-20 are termed very poor and 20-40 are poor; these values correspond to very low values of cohesion and coefficients of friction (Bienawski, 1989,1993). Drill data were originally reported in imperial system measurements and have been changed to metric measurements for this paper. From the RMR_{1989} data, we calculate Young's modulus and sonic velocities of the rock (see Supplemental File 8 for details).

The up-dip and along-strike parts of the SGF exposed in Little and Big Tujunga Canyons (Figure 2) were sampled by J. S. Caine in 1993 and 34 thin sections were prepared in 1994. Data and images for 22 hand samples of these exposed rocks and thin sections (Supplemental file 3) and field notes (J. S. Caine, pers. comm, 2021) establish their provenance relative to the faults and provide small-scale structural data. These field sites are discussed in Anderson et al. (1983) and Supplemental File 3.

We used optical microscopy to examine grain-scale deformation and the textural composition of the fault-related rocks, the relationships of grains to surrounding material, and the evidence for the interaction of minerals, shearing, and fluid-rock interactions (Schulz and Evans, 1998; Bradbury et al., 2015). Standard (27 x 46 mm x 30 μm) and 11 large (51 x 77 mm x 30 μm) probe polished thin sections from the ALT-B2 core, 26 standard and 8 large thin sections from the field samples were examined. Entire thin-section scans were made using an Epson Perfection Pro scanner in plane-polarized and cross-polarized light.

Systematic X-ray diffraction (XRD) analyses were done to determine whole-rock mineralogy and to constrain rock compositions, depth ranges, and fluid-rock interactions in the fault-related rocks. Fluid-rock interactions alter the mineralogy of rocks (Warr and Cox, 2001; Callahan et al., 2020), and mineralogic variations (Ishikawa et al., 2008; Ishikawa, 2014) can indicate the nature of the fluids that may have interacted with the rocks. Field, protolith, damage zone, and principal slip zone samples were sub-sampled to document minute changes in mineralogy, variations in distance from the principal slip surface, slip surface compositions, and relative abundances. Whole-rock geochemical data and X-Ray Fluorescent maps of thin sections of these samples are discussed in Evans et al. (submitted). The sample locations, their descriptions, and X-ray diffraction data summaries are provided in Supplemental File 1.

3. Results

3.1 ***Macroscopic Descriptions***

The host rock of the ALT-B2 core consists of Mendenhall Gneiss on the north side of the fault zone to 313 m measured depth (mmd) along the borehole, with minor igneous intrusive rocks, and Josephine Granodiorite from ~313 mmd to the bottom of the borehole (Figures 3 and 4) on the south side of the fault. Two principal slip zones are recorded in the ALT-B2 core, corresponding with indurated fault/clay gouge recorded at 313-325 mmd and 456.5-476.5 mmd along the borehole (Figures 3 and 4). The upper principal slip zone at 313-325 mmd coincides with the lithologic change from the gneissic rocks to the north and the granodiorite to the south of the SGF. We interpret this as the main fault zone, as do the geologists in the draft geotechnical report (California High-Speed Rail Authority, 2019). Correction for the obliquity of the drill hole suggests that this principal slip zone has a true thickness of about 6.5 m. The lower principal slip zone is 11 m thick. It is embedded within the Josephine Granodiorite and may define a margin of the damage zone of the SGF. The drill hole did not continue beyond this zone, however, so that relationship is not certain (Figure 3). The lowermost ~ 20 m of the borehole encountered the third zone of low RMR_{1989} values.

Fracture data presented in the geotechnical study (Supplemental File 2) documents the nature and distribution of fractures along the borehole. Fracture density varies from slight to very intense (Figure 3; Figure S2.3A), and fracture dip increases with depth (Figure S2.3B). Zones of high fracture intensity are found at 140-160, 200-230, and 340-370 mmd. The fracture spacing is relatively less intense directly north of the principal slip zones, with a ~40 m wide zone of slight-moderate intensity north of the upper principal slip zone and a 15 m wide moderate intensity zone north of the lower principal slip zone (Figure 3; Figure S 2.3A). The rocks in these lower-intensity fracture zones have higher RMR_{1989} values and exhibit evidence for shearing and folding, described below, with few preserved fractures and veins. We observe lozenges of relatively unaltered to slightly altered protolith around 61 m and 25-30 m north of the main SGF trace (at 251 mmd and 280-288 mmd in the borehole).

The rocks in the ALT-B2 borehole exhibit fault damage zones that extend ~60 m to the north and ~ 30 m to the south of the upper principal slip zone. The damage zones are defined by intense to very intense fracture spacing, the presence of sheared rock (Figure 4; Supplemental File 4), and altered and damaged rock assemblages. Zones of poor to very poor RMR_{1989} values (<40) are recorded at 104-120 mmd, 145-160 mmd north of the upper principal slip zone in ALT-B2, a zone up to 60 m south of the upper principal slip zone (310-390 mmd), and a zone at 405 to 416 mmd. Numerous zones of low RMR_{1989} are found through the borehole (Figure 3), including at the principal slip zones of 313-325 mmd and 456.5-476.5 mmd. Low RMR_{1989} values indicate that these zones consist of a combination of low uniaxial compressive strength, high fracture spacing, fracture orientations, high water saturation, and poor drill core recovery (Bieniawski, 1978, 1989).

Field exposures of the San Gabriel Fault south-southeast of the drill site (Figure 5; Supplemental Files 3 and 5) provide context on the fault orientations, related fault structures, and samples for microstructural analyses. At the Little Tujunga Canyon sites (Supplemental File 3) the fault is exposed at two sites; at LT 1 (site 7 of Anderson et al., 1983) the fault juxtaposes slivers of Eocene (?) sedimentary rocks (Dibblee and Ehrenspeck 1991) and the Josephine granodiorite on the north across an ~ 4 m thick zone with 1-4 cm thick cataclasite zone that dips steeply southwest (Figure 6 A-C). Closely spaced fractures or cleavage-like planar fabric is present within the fault zone, which is variably mapped here as comprising one or several strands along the strike (Dibblee and Ehrenspeck, 1991). At sites LT2 (Figure 5: site 8 of Anderson et al.,1983; the Earthquake Fault Interpretive site) the fault exposes Mendenhall Gneiss to the northeast on Josephine Granodiorite to the southwest (Anderson et al., 1983) on a steep northeast-dipping fault (Figure 6 D). At both sites, the fault core is composed of a 1-4 cm thick dark brown to black ultracataclasite zone (Figure 5 C; Anderson et al., 1983; J. S. Caine, written comm., 2019). The Josephine Granodiorite is highly fractured and altered up to 15 m away from the fault core. The small faults and fractures are mostly at high angles to the main fault surface (Figure 6 A, B) and quartz and epidote veins are subparallel to the main fault strand (Figure 6C). At site LT2, the damage is expressed primarily as fractures at a range of orientations. Veins are subparallel to the fault (Figure 6D) and zones of alteration in the gneiss. At ~ 5-6 km east-southeast of the LT1 and 2 sites, roadcuts reveal a series of steeply southwest dipping faults that are several meters to ~ 17 m thick (Supplemental File 3).

Fracture density as determined from the acoustic image logging tool run in the borehole (Figures 6E, F) show that fractures in the rocks, accounting for the sampling bias along a linear traverse (Terzaghi, 1965), are concentrated in two groups. Most fractures dip moderately northeast and strike northwest, and a subordinate group dips steeply southwest and strikes southeast. Fracture dips show a slight trend of increased dips with depth (Supplemental File S 2.4), but as in the core data, the changes are slight.

Big Tujunga sites BT 1, 2, and 4 (Sites 10, 11, and 14 of Anderson et al., 1983) reveal the North Branch of the San Gabriel Fault is exposed in a series of fault strands in weathered outcrops ~ 1 km east of the branch point with the South Branch of the fault (Supplemental File 3; Dibblee and Carter, 2002; Ehlig, 1973). The fault zone here juxtaposes Cretaceous (?) quartz diorite and granodiorite (the Wilson Diorite of Wilson, 1934) on the southwest side of the fault, and Cretaceous quartz monzonite and granodiorite, and the Josephine Granodiorite to the north (Dibblee and Carter, 2002). Here the fault zone is an up to 4-7 cm thick cataclasite with a 70 m thick foliated shear zone that dips steeply southwest (Supplemental File 3). One sheared sequence is ~ 6m thick and consists of an anastomosing network of brecciated fault clasts in a zone of polished and striated slip surfaces. In places, 2- 5 m thick zones are composed of chloritically altered granodiorite and altered quartz monzonite. Thin, 5-10 cm thick black and dark brown fault zones are composed of foliated gouge and ultracataclasites and show sharp boundaries with damaged rocks. The likely main fault zone dips steeply southwest, and the few related slip surfaces dip steeply around the main fault surfaces (Figure 5E). At the eastern end of the outcrop at BT2, a fault strand is as much as 40 m thick with a fault-related foliation that dips steeply north.

3.2 *Mesoscopic Observations*

We divide the drill core samples into protolith, damage zones, and principal slip zones (Caine et al.,1996; Wibberley and Shimamoto, 2003) based on mesoscopic observations (Supplemental File 4), geotechnical reports, and distance from the principal slip surface (Figures 4 and 7). The rocks in the upper part of ALT-B2 consist of slightly to moderately deformed protolith of the felsic Mendenhall Gneiss (Figure 4A). These rocks exhibits cm-scale gneissic banding defined by feldspar-rich and hornblende ± biotite rich layers. The damaged zones exhibit fault-damaged rocks with fractures, brecciated zones, veins, folded cataclasites, shear zones, and cataclasites (Figure 4B-G). The damage zone rocks consist of cm- to 5+ cm thick clay-rich zones that envelope quartzo-feldspathic blocks (Figure 4B), clay-rich shear zones with elongated lozenges of carbonates (Figure 4C), and breccia zones composed of angular fragments and cut by fractures (Figures 4D and 7E). The principal slip zones consist of cataclasite, ultracataclasite, and moderately indurated clay gouge proximal to and within the fault (Figure 4F). The zone we interpret as the fault core is ~6.5 thick measured perpendicular to the fault zone, and is comprised of black aphanitic gouge material with mm- to cm-scale angular to rounded fragments of brecciated and altered fragments of gneiss. In the south block of the fault zone, in deformed Josephine Granodiorite, the damage zone from ~320 to 440 mmd consists of rocks that experienced significant deformation and alteration (Figure 4G). Alteration is indicated by the light- to medium-green chloritic rocks, and pink, white, and red fine-grained materials that suggest the presence of carbonates, iron-oxides, and hydrothermally altered feldspars. The borehole does not sample undamaged igneous rock from the Josephine Granodiorite, but outcrop samples sample relatively undamaged rock from the Josephine Granodiorite and the Mendenhall Gneiss at the surface.

Drill core samples are highly indurated and the core recovery rate was 95% (Supplemental File 3). The 0.9 m of gneissic protolith from 4 different sites show gneissic banding 0.2-2 cm thick and feldspar (primary albite to oligoclase) and hornblende-dominated mineralogy with slight to moderate damage. Gneissic protolith samples are differentiated from damage zone samples by the presence of well-defined gneissic banding of altering light and dark bands and minerals that are easily recognizable (Figures 7A, B). The Mendenhall Gneiss experienced high-grade Precambrian granulite-grade and Mesozoic greenschist-grade metamorphism (Anderson et al, 1983).

Damage zone samples exhibit breccias, cataclasites, shear zones, penetrative shear fabrics, fractures, veins, iron oxide-coated fractures, mm-wide veins, and discrete slip surfaces, with many samples showing multiple types of deformation (Figures 7C-H). Sheared samples in the damage zones directly north of the upper and lower principal slip zones (Figures 3) exhibit folding of foliated cataclasite and penetrative shear fabrics, with generally fewer and smaller preserved veins (Figures 7D, F, H). Some veins in the sheared rock show cross-cutting relationships with existing cataclastic foliations (Figure 7F). Veins visible in the Josephine Granodiorite damage zone south of the upper principal slip zone are larger and more abundant than those preserved in damaged rock in the Mendenhall Gneiss north of the upper principal slip zone, with veins up to 1.5 cm wide and >20 cm long (Figure 6C). The drill core in the granodiorite damage zone tends to be slightly less indurated than the drill core from the gneissic damage zone (Supplemental File 3).

The 0.5 m of principal slip zone core samples from 4 sites, two in the principal slip zone at 313-325 mmd and two in the lower principal slip zone at 456.5-476.5 mmd, reveal that samples from the upper principal slip zone exhibit cataclasites, shear surfaces, and fractures (Figure 7I). The samples from the lower principal slip zone exhibit very fine-grained fault-related rocks such as ultracataclasite and relatively well-indurated clay fault gouge (Figure 7J). The rocks from the field sites (Figure 8; Supplemental File 5) range from protolith Josephine granodiorite (Figure 8 A and B), foliated and fractured gneiss (Figure 8C), indurated leucocratic breccias and cemented cataclasites (Figure 8 D, E), indurated chloritic cataclasite (Figure 8 F, G), and aphanitic ultracataclasite (Figure 8H).

3.3 ***Microstructures and alteration textures in core***

Thin sections span the length of the ALT-B2 borehole and sample each rock type identified in the drill core (Figures 9-14; Supplemental File 6). We further divide the rocks described here into protolith, upper damage zone rocks from north of the upper fault, highly sheared rocks from the upper damage zone, samples from the upper fault zone, rocks from the lower damaged and altered zone, and samples from the lower fault zone. The protolith samples consist of slightly to moderately fractured gneiss, with quartz, relatively unaltered feldspar, biotite, and hornblende grains (Figure 9). In parts of the gneiss, the foliated fabric is largely absent (Figures 9A and B) and the rocks consist of hornblende- plagioclase-rich zones, and in places, mafic-rich zones have rounded leucocratic enclaves (Figure 9B). Gneissic foliation of the Mendenhall Gneiss in the core is defined by 0.1 to 3 cm wide bands of leucocratic and mafic mineral zones (Figures 9C and D) with varying amounts of mafic mineral concentration. The Mendenhall Gneiss exhibits retrogression in which original pyroxene and garnets are replaced by hornblende + biotite + calcite + epidote + quartz (Barth et al., 1995). The protolith gneiss is cut by thin intra- and intergranular fractures with no or 1-2 preferential directions, discrete slip surfaces, and quartz or calcite, veins (Figure 9A, C). Undeformed Josephine intrusive suite samples from field sites (Figure 9E-H) consist of diorite, tonalite, and granodiorite (Barth and Ehlig, 1989) intruded at depth of ~ 20km. The Big Tujunga samples reveal equant-to-subsequent quartz grains in altered feldspars (Figure 9 E, F), elongated zones of hornblende + biotite, and evidence of retrogression of the feldspars and hornblende-biotite regions (Figure 9F). Slip surfaces that cut the granodiorite appear to link transgranular fractures that link the feldspar and mafic mineral zones (Figures 9 G, H).

Damage zone samples show a range of deformation microtextures and fabrics such as the presence of foliated cataclasites, breccia, shear zones, fractures, veins, zones of chloritization, and Fe-oxide-rich slip surfaces and zones (Figure 10). Damaged and altered fault-related rock in the gneiss has brittle fractures, zones of chloritic alteration (after biotite), calcite veins, clays, and zeolite masses, and cementation textures that disrupt the mafic zones (Figure 10A). Foliated cataclasites show banding of concentrated iron oxide, calcite, and/or clay-rich material and brecciated and deformed host rock (Figure 10B). Cataclasites exhibit a chlorite-rich folded and refolded folia, some disarticulated, juxtaposed against breccia (Figure 10C). Breccia samples exhibit Fe-oxide/chlorite- and microbreccia-rich matrices and the cementation of quartzofeldspathic grains, with quartzofeldspathic clasts exhibiting micro- and intragranular fractures and mosaic fracture textures (Figure 10D). Many of the primarily hornblende grades are degraded to chlorite in the damage zone.

Highly sheared rocks from the upper damage zone (Figure 11), 30 to 50 m from the upper principal slip surface, exhibit a range of alteration and deformation textures. The rocks exhibit mm-thin slip surfaces (Figure 11A) that cut foliated cataclasite and white cemented cataclasite (Figure 11A). These ultracataclasites contain rounded to elongated fragments of host cataclasite (Figure 11B). Alteration and mineralization in the damage zone consist here of carbonate and zeolite mineralization, lozenges of which are incorporated in the sheared rocks, with elongated to rounded fragments in the dark sheared materials (Figure 11C). These mineralized zones show evidence of deformation of these altered zones, with elongate fragments comprised of carbonate and zeolite layers in porphyroclasts of laminated horizons of clay-rich sheared surfaces (Figure 11C) elongate parallel to the foliation defined by iron oxide and clay-rich layers. Iron-oxide-rich slip surfaces manifest as very thin to mm-thick slip surfaces that sometimes appear to have been injected into surrounding material (Figure 10B-D). Veins are composed of quartz, calcite (Figure 11), chlorite, and Fe-oxide. Cross-cutting relationships can show evidence for multiple generations of veins and display overprinting of brittle and plastic deformation events (Figure 11). Veins in samples from the damaged Josephine Granodiorite south of the main principal slip zone are frequent and visible at the mesoscopic level, with veins up to 1.5 cm wide and >20 cm long, while veins in the damaged rock north of the main principal slip zone are mostly visible only at the microscale. Mechanically twinned calcite is pervasive throughout the damage zone, visible in veins and clasts of calcite, and is commonly cross-cut by brittle fractures and veins.

The upper principal slip zones consist of cataclasite, ultracataclasite, and relatively well-indurated clay gouge (Figure 12). The main principal slip zone exhibits zones of chloritization, cemented microbreccia and breccia, and intergranular fractures (Figure 12A). Quartzofeldspathic clasts that lie in a Fe-rich matrix are angular to subrounded and exhibit intragranular fractures, and in some cases appear to be fragments of the damage zone. The lower principal slip zone consists of clay fault gouge and ultracataclasite with intergranular fractures and penetrative cataclastic texture. The clay fault gouge exhibits highly fractured, and possibly cemented, quartzo-feldspathic damage zone clasts showing the effects of early cataclasis, healing, and further shearing and alteration.

The lower damage zone is entirely in the Josephine granodiorite and is comprised of highly sheared, altered, and mineralized rocks (Figure 13). Cataclasites consist of quartz fragments, some of which exhibit undulose extension, in a matrix of fine-grained deformed feldspar fragments, with narrow black slip zones (Figure 13A). Foliated deformed and veined rocks (Figure 13 B-F) exhibit evidence for carbonate mineralization in very fine-grained microbreccia (B), and carbonate fragments lie within the cataclasites. Wide calcite veins (Figure 13 C) attest to high pore-fluid pressures that created mineralized Mode I fractures. Cross-cutting relationships indicate that breccias formed early, followed by fine-grained cataclasites, cut by carbonate veins, which are cut by narrow slip surfaces (Figure 13D). In some cases, carbonate mineralization occurred early and resulted in sheared carbonate fragments in a foliated rock cut by a very thin slip surface or solution seam (Figure 13E).

The lower principal fault zone is comprised of extremely foliated and fine-grained material (Figure 14) that appears to be ultracataclasite. Rocks from ~ 15 m from the fault zone consist of foliated, interlayered zones of catacalasite and carbonate and zeolite-rich altered rocks (Figure 13E) while subsequent brecciation created fragments of the altered rock entrained on the cataclasite. These rocks are overprinted by thin dark bands that might be solution seams or slip surfaces. Ultracataclasite is preserved in the fault zone (Figure 14A) where dark, aphanitic sheared rock exhibits several different colors and have distinct sharp boundaries, with some foliation visible. Deeper in the borehole, the dark aphanitic matrix has rounded clasts of protolith, most of which exhibit carbonate mineralization (Figure 14B) in the foliated fine-grained matrix.

Samples from the field sites (Figure 15; Supplemental File 7) support the observations in the core where we can see the key rock units in and around the fault (Figure 5). Fault core samples exhibit foliated cataclasites (Figure 15B) and fine-grained gouge that contains clasts of earlier formed gouge (Figure 15C). The damage zone consists of a ~ 1m thick zone on either side of the fault slip zone, where the rocks are cut by fractures, sheared chloritic and iron-oxide zones with irregular foliation (Figure 15A). The host gneisses are relatively undeformed and unaltered (Figure 15D). Samples from the fault core at the LT 1 site also have multigenerational gouge textures – clasts of fine-grained gouge and cataclasite in a matrix of gouge (Figure S7.5).

Samples from the BT sites provide examples of deformation of the Josephine Granodiorite and the textures of alteration, mineralization, and shearing that are similar to those observed in the core samples (Figure 15 E-H). The equigranular quartz-feldspar-biotite-amphibole granodiorite exhibits distributed zone of thin sheared zones and zones of distributed sheared gouge (Supplemental File 6). Altered sheared cataclasite, mineralized by calcite and zeolite veins and by grain-scale alteration (Figure 15E). Veins are discrete, distributed, or are large irregular zones (Figure 15F). Highly sheared textures Figure 15G) consist of layers of altered cataclasite and sheared carbonate-zeolite veins. The protolith (Figure 15H) here consists of foliated gneiss cut by small faults.

3.4 *Mineralogy*

The X-Ray diffraction analyses of the borehole samples (Table 2; Supplemental File 7) document the mineral assemblages in the protolith, damage zones, and principal slip zones. The Mendenhall Gneiss protolith consists of quartz, feldspar (albite and anorthite), amphibole, muscovite, biotite, and phlogopite. Barth et al. (1995) show that in some places, unaltered mafic zones consist of pyroxenes and plagioclase, and commonly these zones are altered to hornblende+ biotite± calcite+ epidote+ quartz, and we find Mg and Fe-oxide minerals in these rocks as well. Due to the lack of unaltered granodiorite protolith samples in ALT-B2, we rely on the work of Anderson (1983) and Barth et al. (1995) for primary mineralogy analyses. The Josephine Intrusive suite rocks consist of quartz, alkali feldspars, and lesser amounts of hornblende and biotite. Common alteration minerals in the upper damage zone consist of phlogopite, chlorite, calcite, and iron oxides. The upper principal slip zone includes calcite, clays (nontronite, glauconite), metal oxides (Fe and Mg, with traces of Zn, Sr, Mn), zeolites, and minor epidote. The lower damage zone contains laumontite, calcite, chloritic minerals, calcite, and clays (Table 1) and the principal slip zone exhibits Na-clays, micas, calcite, and zeolites.

4. Discussion

The data from this analysis of samples from the CHSRA ALT-B2 borehole across the North Branch of the San Gabriel Fault, within the context of other work (Anderson et al., 1983; Chester et al., 1993; Evans and Chester, 1995; Evans et al., submitted; Crouch et al., in prep.), enables us to define the mesoscopic structure of the fault and the nature of and the relationships between rocks and physical properties of the fault-related rocks.

4. 1 San Gabriel Fault Zone Structure

The data from the ALT-B2 borehole documents the presence of two principal slip zones: an upper 6.5 m thick principal slip zone (Figure 3) at 313-325 m measured depth, and an 11-m thick lower fault zone at 456.5-476.5 m measured depth. The upper fault is consistent with interpreting it as the down-dip continuation of the surface trace of the fault (Figures 5 and 6), evidenced by the fault geometry, inclination of the borehole, the dip of the SGF, and the juxtaposition of the host rock Mendenhall Gneiss and Josephine Granodiorite in the borehole (Figure 3; d'Alessio. 2004). The cataclasite samples we examine in the 6.5 m thick upper principal slip zone match descriptions of the surface expression of the SGF, which describes the principal slip zone (termed the "fault core" in Chester et al. (1993) and Evans and Chester (1995)) of the SGF as m-thick cataclasite and cm- to m-thick ultracataclasite (where present) (Anderson et al. 1983, Chester et al. 1993, Evans and Chester 1995).

Along strike, and down dip, the San Gabriel Fault zone varies from a single fault zone with a narrow principal slip surface to a zone with multiple fault surfaces (Figure 5; Supplemental File 3; See Anderson et al., 1983; Dibblee, 1991; Dibblee and Ehernspeck, 1991; Dibblee and Carter, 2002; Yerkes et al., 2005; Campbell et al., 2014). The lower fault zone in the ALT-B2 borehole is thus likely a branch of the SGF. The 11-m thick lower principal slip zone exhibits indurated clay fault gouge and ultracataclasite, suggesting fault maturity in the formation of these ultrafine-grained fault-related rocks. The penetrative ultracataclasite we document is similar to those described in the SGF by Chester et al. (1993) and Evans and Chester (1995).

The total width of the fault zone recorded by borehole ALT-B2 is nearly 200 m, with ~60 m on the north side of the SGF, ~50 m between the two principal slip zones, and an unknown amount below the extent of the borehole. The borehole does not sample beyond the lower principal slip zones and another ~100 m of damage is likely to present there. The lower principal slip zone is more brittlely deformed than the upper principal slip zone and it could be embedded within a damage zone that exceeds 100 m in width. The presence of indurated clay-rich gouge, foliated cataclasite, well-developed ultracataclasite, and the nature of hydrothermal alteration in the lower fault zone (see below) suggests the lower fault zone may be the mature strand here and may have been responsible for a significant fraction of overall slip. Dibblee and Ehernspeck (1991) show the De Mille Fault (Weber, 1982), a Quaternary-late Tertiary fault that forms the southern boundary of an ~ 10 km long, up to 1.4 km wide fault zone, bounded by the San Gabriel Fault (*senso stricto*) on its northern side. The upper, southwestern fault encountered in the ALT-B2 borehole may be the subsurface expression of the DeMille fault as it merged with the San Gabriel Fault.

The damage zone between the two principal slip zones exhibits an approximately 50 m thick zone of low RMR values, intense brittle deformation, and slightly less induration than the highly fractured and sheared sections of Mendenhall Gneiss damage zone north of the upper trace of the

SGF. Mesoscopic fractures and veins in the Josephine Granodiorite damage zone south of the SGF are up to 1.5 cm wide and >20 cm long, suggesting variances in fluid-rock interaction throughout the SGF.

The borehole contains a ~40 m thick zone of macroscopically 'ductile' and highly sheared fault-relate rock in the drill core. Lozenges of protocataclasite in the drill core of the gneissic damage zone directly north of the principal slip zone (Figures 3-5; 7-9) transition to and above the lower principal slip zone in the granodiorite exhibit significant amounts of shearing (Figures 7 D, F). The drill core in these zones has fewer discrete fractures and exhibits fine-grained, clay-rich foliated sheared rock. The presence of these zones of fine-grained, shear-dominated deformation may be the result of asymmetric seismic energy propagation in the fault zone that may be exacerbated in the case of the upper principal slip zone in part due to differences in protolith on either side of the fault (Ben-Zion and Huang, 2002; Mitchell and Faulkner, 2009; Faulkner et al., 2011). Damaged and altered rocks within these lower fracture intensity zones can show multiple generations of folds and re-folds of cataclasites, implying the accommodation of ductile deformation over the course of a significant period (Figure 11C).

4.2 *Physical properties of the fault-related rocks*

The mechanical behavior of fault zones over the seismic cycle (Rice, 2006) and their impacts on the nature and degree of seismic energy propagation (Kanamori and Rivera, 2006) and radiation (Roten et al, 2017) are a function of the material properties of the faults. The compiled RMR_{1989} data (Figure 3) assigns a value for the quality of the rock used to estimate its ability to withstand failure under a range of engineered load conditions (Bieniawski, 1989, 1993). The RMR_{1989} factor (and all other rock-mechanics-based rock quality measures) combine measures of fracture density and conditions, the type of rock, and various relatively simple rock mechanics measurements of rock strength, such as unconfined compressive strength, to estimate macroscopic rock strength (Supplemental File 8). These factors can be used to estimate elastic Young's moduli of the rock masses E_m, uniaxial compressive strength (C_u), coefficients of friction (μ), and Poisson's ratio (ν) via correlations based on experimental measurements (Supplemental file 8; Bieniawski, 1989; Aydan et al., 2014). The highly sheared rocks in the fault zone have RMR values < 40, and in the two fault zones, RMR is as low as 20 or lower (Figure 3). Based on a range of correlations (Aydan et al., 2014; Supplemental Files 3 and 8: CHSRA, 2019), we estimate the mechanical parameters for the *in situ* properties of the San Gabriel fault-related rocks to consist of 1-5 m thick zones of alternating high- and low-magnitude Young's moduli above the faults zone. Very weak rocks comprise the damage zones in and around the fault zone (Table 3), where the three damaged zones have Young's moduli of 1-5 GPa, two to four times less than that of rocks at the same depths outside the fault zone (Figure S 8.2).

We estimate the values for the compressive and shear-wave velocities in the rocks (Jeppson et al., 2010; Mavko et al., 2020), where

$$Vp = \sqrt{\frac{E(1-\upsilon)}{\rho(1+\upsilon)(1-2\upsilon)}} \tag{1}$$

and

$$Vs = \sqrt{\frac{E}{2\rho(1+\nu)}} \tag{2}$$

The calculated P-wave velocities above the fault zone range from 1000-3500 m/second, with a general decrease towards the upper fault zone and interleaved zones of higher and lower velocities (Figures S8.3 and 16). The S-wave velocities are between 600 to 2000 m/s above the fault zone. The 5-10 m thick zones of low RMR result in alternating zones of higher and lower velocities above the fault. The three damaged zones are regions of extremely low velocities – 600-1000 m/second for V_s and 1000-1700 m/second for V_p (Figures S 8.3 and 16). These values 30-50% of relatively intact rocks observed in the ALT=B3 borehole, where velocity logs define an upper zone of V_p of 3000-4000 m/sec, and V_s of 1000 to 1200 m/sec. Lower in the section, the granodiorite protolith exhibits velocities of 4000-5000 m/sec (V_p) and ~ 2000 m/sec V_s. The ALT-B2 rocks (Figure 16) show that the fault zones are associated with low Vp/Vs values and the ratios are higher in the fault zones. These data indicate that the fault zones contain pore fluids,

4.4 Summary and Conclusions

The macroscopic to microscopic deformation and alteration patterns in the fault-related rocks of the San Gabriel fault (Figure 16) shows that the damaged zones of the upper of the San Gabriel fault document the interplay of deformation and alteration of the rocks. This alteration, marked by the development of clays, zeolite minerals, and calcite, and the geochemical variations (Figure 16; Evans et al., submitted) marks the presence of the damage zones and results in the low V_p and V_s values. We suggest the majority of coseismic slip is localized to the principal slip zones as documented by the fine- and ultrafine-grained deformed rocks of cataclasite, clay gouge, and ultracataclasite (Chester et al. 1993, Evans and Chester 1995).

The folded and layered cataclasite textures in the clay-rich fault-related rock likely formed in the rock's systematic shearing and aseismic deformation. Evidence for multiple generations of folding, cataclasite development, and vein formation indicate prolonged periods of brittle deformation. Rootless and elongated calcite lozenges in plastically sheared material as indicators for the systematic ductile shearing of altered fault-related rock.

Seismic and aseismic indicators are recorded locally within the same samples and show evidence for complex overprinting of brittle and ductile deformation fabrics. The presence of folded cataclasites and twinned calcite juxtaposed against fault breccia (Figure 13) indicates a complex history that includes the formation of cataclasite, the reworking and folding of the cataclasite, the formation of the breccia, and the truncation of the folded cataclasite and breccia by slip surfaces. The pervasiveness and cross-cutting nature of seismic and aseismic alteration and deformation textures recorded throughout the sampled SGF reveals a complex interplay and overprinting of both mechanisms throughout the earthquake cycle during the formation of these fault-related rocks at depths of ~2-2.5 km. We infer that both seismic and aseismic mechanisms are integral in shallow fault processes and must therefore be accounted for in fault and earthquake models. This is supported by analyses of fault-related rocks that formed at 2-3 km depth in the San Andreas Fault (Studnicky et al., 2021), the San Gabriel Fault (Anderson et al., 1983), and other faults that recorded similar results (Gratier et al., 2003; Bradbury et al., 2015; Marone and Saffer, 2007; Boulton et al., 2017; Holdsworth et al., 2011; Jeffries et al, 2006; Mitchell and Faulkner, 2009; Faulkner et al., 2003; Williams et al., 2021).

The elastic and seismic velocity properties of the fault zone indicate that the fault zone consists of three weakened zones of low velocities and elevated pore-fluid content 20-50 m thick, and slivers of weakened rocks above the main fault zone. These zones would reach their yield strength at low stresses, enable slip to be distributed across the zones, and be regions where seismic energy could be readily dissipated.

Characterizing the behavior and structure of shallow faults are needed to model earthquake hazards and seismic energy dissipation (Kaneko and Fialko, 2011; Roten et al., 2017). Our data records pervasive and cross-cutting brittle and ductile deformation textures, indicating influence from seismic and aseismic deformation mechanisms within the deformed and altered shallow San Gabriel Fault. These data document the need to consider both mechanisms when modeling fault and earthquake behavior over the entire depth range of fault zones. Observations and data quantification made here on the SGF may serve as an analog to help decipher the nearby active San Andreas fault and similar faults.

Acknowledgments

This work was funded by NSF grants EAR-920577 and 1824852, SCEC grant 18077, and USGS-NEHRP grant 1434-92-G-2184 to Evans. Grants from the Geological Society of America - Continental Scientific Drilling Division, American Association of Petroleum Geologists L. Austin Weeks, a Utah State University Academic Opportunity, URCO, Peak Summer Research Fellowship, and a College of Science grants supported Kaitlyn Crouch. Many thanks to Caroline Studnicky for the initial collection of core samples, to Kathlien Red (Kleinfelder) and Randy Anderson (CHSRA) for help accessing the core in 2019, and to Paul Guptill (Kleinfelder) and the California High-Speed Rail Authority for accessing the geomechanical data from the borehole released by the under California High-Speed Rail Public Records request # 22-164. Field data, sample collection, and outcrop photos by Jonathan Caine, David Forand, and Joseph Jacobs, and photography of samples by Roxie Crouch is gratefully acknowledged. Steven Schulz prepared field samples for thin section study. Reviews of earlier versions by xxx helped us improve the paper.

Author Contributions

Crouch, Caroline Studnicky, and Evans sampled the core in 2018 and 2019. Crouch examined the core in detail, recompiled the fracture spacing and RMR data from the borehole data provided by Kleinfelder, performed all of the microstructural studies, examined and interpreted the thin sections, performed the X-Ray diffraction studies, compiled and curated all of the data sets, including all of the images, and integrated and interpreted the data for this paper. Evans collaborated with Crouch on these efforts, made the calculations for the elastic and seismic properties, and edited the initial drafts of the paper with Crouch and Janecke. Evans and Steven Schulz prepared the outcrop samples for thin sections.

Core Box	Core sample name	Measured Depth ALT-B2 From (m)	To (m)	Distance from PSS along ALT-B2 (m)	Horizontal distance from PSS (m)
11	SGF11	55.87	56.05	257.1	138.4
28	SGF28	127.71	127.88	185.3	99.7
39	SGF39	177.45	177.70	135.5	72.9
45	SGF45	202.94	203.00	110.1	59.2
49	SGF49	223.17	223.27	89.8	48.3
51	SGF51	229.54	229.70	83.5	44.9
54	SGF54	244.36	244.60	68.6	36.9
56	SGF56	251.00	251.19	62.0	33.4
59	SGF59A	266.70	266.84	46.3	24.9
59	SGF59B	266.84	266.95	46.2	24.8
59	SGF59C	266.95	267.01	46.0	24.8
60	SGF60.1	267.31	267.45	45.7	24.6
60	SGF60.2	269.81	270.05	43.2	23.2
63	SGF63	281.57	281.80	31.4	16.9
64	SGF64	287.91	288.22	25.1	13.5
65	SGF65A	291.24	291.51	21.8	11.7
65	SGF65B	291.51	291.74	21.5	11.6
65	SGF65C	291.65	291.80	21.4	11.5
66	SGF66	295.85	295.95	17.1	9.2
70	SGF70	314.61	314.78	1.6	0.9
71	SGF71	315.86	316.00	2.9	1.5
80	SGF80	360.73	360.85	47.7	25.7
92	SGF92	408.43	408.65	95.4	51.4
93	SGF93.1	413.26	413.48	100.3	54.0
93	SGF93.2	413.52	413.64	100.5	54.1
93	SGF93.3	416.28	416.45	103.3	55.6

94	SGF94.1	417.32	417.52	104.3	56.1
94	SGF94.2	418.87	418.96	105.9	57.0
95	SGF95	420.76	420.85	107.8	58.0
96	SGF96	426.28	426.43	113.3	61.0
103	SGF103	456.44	456.53	143.4	77.2
107	SGF107	472.27	472.41	159.3	85.7

Table 1. Summary of the location of the core samples for this research. Drill runs are recorded as the box number and the nomenclature of the sample names (see Figure 3) are tied to these numbers. Depths of the samples, originally measured in feet and converted to meters, are shown, and these are used in conjunction with the entire core logs (CHSRA, 2019) to constrain the subsurface geometry of the fault zones.

Drill Core Run	Sample	Major minerals	Minor minerals	Present	Rock Type	Measured Depth (m)
11	11.2	Quartz, Albite	Muscovite, Biotite, Anorthite	± Sulfides	Protolith	55.9
28	28.2	Quartz, Albite	Zeolite, Actinolite		DZ	127.7
39	39.1	Quartz	Albite	Phlogopite, ± sulfate	DZ	177.5
39	39.2	Quartz	Albite, Clay	Zeolites (laumontite), Mg oxide, ± Sr oxide?	DZ	177.5
49	49	Iron Oxide	Quartz, Nontronite, Albite, Mg Oxide	Calcite	DZ	223.2
51	51.2	Albite	Quartz, Calcite		DZ	229.5
51	51.3	Quartz, Albite	Biotite, Anorthite	Clay, ± Fe oxide	DZ	229.5
54	54.2	Quartz	Albite, Calcite	Muscovite, ± K-Mn Oxide	DZ	244.4
54	54.3	Quartz, Analcime	Albite	Zeolite , Mg-Fe silicate and oxide	DZ	244.4
56	56	Quartz, Albite, Phlogopite	Biotite	± Na-Al Silicate	Protolith	251
60.1	60.1-1	Quartz, Clay	Chloritic-serpentine, Biotite, Muscovite		DZ	267.3
60.1	60.1-2	Quartz	Albite, Phlogopite	Clay, ± Phosphate	DZ	267.3
60.2	60.2	Quartz	Albite	Phlogopite	Protolith	269.8
63	63-1	Quartz	Albite, Phlogopite		Protolith	281.6
63	63-2	Quartz	Albite		Protolith	281.6

64	64	Quartz	Mg-Mn Silicate	Biotite, Albite, Phlogopite	Protolith	287.9
65A	65A-1	Calcite	Quartz, Albite, Chloritic-serpentine	Clays	DZ	291.2
66	66.1	Quartz	Albite, Phlogopite, Biotite	± Epidote	DZ	295.9
66	66.2	Quartz	Albite-Ca	Orthoclase, ± Zircon	DZ	295.9
66	66.3	Quartz	Albite, Calcite		DZ	295.9
70	70-1	Quartz	Albite	Phlogopite	PSZ	314.6
71	71-1	Quartz	Albite, Calcite	± Mg oxide	PSZ	315.9
71	71-2	Quartz	Albite, glauconite	Calcite, Zeolite	PSZ	315.9
80	80.1	Quartz	Albite-Ca	Laumontite	DZ	360.7
80	80.2	Quartz	Albite	Laumontite	DZ	360.7
93.1	93.1	Quartz	Albite-Ca, zeolite (Co-Al phosphate)	Anorthite	DZ	413.3
93.2	93.2	Quartz	Albite-Ca, Orthoclase		DZ	413.5
93.3	93.3	Quartz	Albite, Calcite, Zeolite		DZ	416.3
94.2	94.2	Quartz	Albite-Ca-zeolite	± oxide, ± calcite/dolomite	DZ	418.9
96	96.1	Quartz	Albite-Ca, chloritic-serpentine, calcite	Clay, Muscovite, Calcite, Mg oxide	DZ	426.3
96	96.2	Quartz	Calcite, Muscovite, Albite, Mica	Clay, zeolite (Na-Al silicate)	DZ	426.3
103	103.1	Quartz	Clay, K-Na mica	Laumontite	PSZ	456.4
103	103.2	Quartz, Albite	Anorthite, zeolite (Na-Al silicate)	calcite	PSZ	456.4
107	107.1	Quartz	Albite	Zeolite ± Cu-As sulfide	PSZ	472.3

Table 2. Summary of the X-Ray diffraction mineralogy analyses of samples showing major, minor, and present minerals. Sample locations are plotted in Fig. 3 and sample details are in Supplemental file 7. DZ = damage zone; PSZ = principal slip zone.

RMR_{1989} value	60	40	20
Young's modulus, E (GPa)	4.5-5.8	2.9-5.6	<1.8 – 3.1
Cohesion, C_o (MPa)	0.2-0.3	0.1-0.2	< 0.1
Uniaxial Compressive strength (MPa)	5	2.5	0.5
Coefficient of friction	0.6 – 0.7	0.45	0.25
Poisson's ratio	0.40-0.45	0.35-0.4	0.32-0.38

Table 3. Estimates of mechanical parameters for the San Gabriel Fault in the ALT-B2 borehole based on the RMR values (Figure 3) and correlations summarized in Aydan et al (2014)) and Bieniawski (1989, 1993). The RMR factor (and all other rock-mechanics-based rock quality measures) combine fracture density and conditions, rock type, and rock mechanics measurements of, unconfined compressive strength, to estimate macroscopic rock strength. These factors can be used to estimate fundamental moduli (E, G), cohesion C_o, coefficients of friction (m), and Poisson's ratio (n) via correlations based on experimental measurements (Bieniawski, 1993; Aydan et al., 2014; Zhang, 2016). The highly sheared rocks in the fault zone have RMR values < 40, and in the two fault zones, RMR < 20 (Figure 3). See Supplemental files 8 for data.

REFERENCES

Allmendinger, R. W., Cardozo, N., and Fisher, D., 2011, Structural geology algorithms: Vectors and tensors in structural geology: Cambridge University Press.

Anderson. J.L., Osborne, R.H. and Palmer, D.F., 1983, Cataclastic rocks of the San Gabriel fault-an expression of deformation at deeper crustal levels in the San Andreas fault zone, Tectonophysics, v.98, p.209-240. DOI:10.1016/0040-1951(83)90296-2.

Aydan, O., Ulusay, R., Tokashiki, N., 2014, A New Rock Mass Quality Rating System: Rock Mass Quality Rating (RMQR) and Its Application to the Estimation of Geomechanical Characteristics of Rock Masses, Rock Mechanics and Rock Engineering, v. 47,p. 1255–1276, https://doi.org/10.1007/s00603-013-0462-z.

Aydan O. , Ulusay, R, Kawamoto, T., 1997, Assessment of rock mass strength for underground excavations ,International Journal of Rock Mechanics and Mining Sciences, v. 34 (3-4), https://doi.org/10.1016/S1365-1609(97)00273-6, p. 18.e1-18.e17.

Aydan O , Kawamoto T., 2001, The stability assessment of a large underground opening at great depth. In: Proceedings of the 17th International Mining Congress Ankara, Turkey, v. 1, p. 277–288.

Barber, D.J., and Wenk, H.R, 1979, Deformation twinning in calcite, dolomite, and other rhombohedral carbonates, Physics and Chemistry of Minerals v.5, p.141–165 https://doi.org/10.1007/BF00307550.

Barth, A.P., and Ehlig, P.L., 1988, Geochemistry and petrogenesis of the marginal zone of the Mount Lowe intrusion, central San Gabriel Mountains, California: Contributions to Mineralogy and Petrology, v. 100, p. 192– 204, https://doi.org/10.1007/BF00373585.

Barth, A.P., Wooden, J.L., Tosda, R.M., Morrison, J., Dawson, D.L. and Hernly, B.M., 1995a, Origin of gneisses in the aureole of the San Gabriel anorthosite complex and implications for the Proterozoic crustal evolution of southern California. Tectonics, v.14, p.736-752. DOI:10.1130/0016-7606(1995)107<0201:CCITPO>2.3.CO;2.

Barth, A.P., Wooden, J.L., Tosdal, R.M., and Morrison, J., 1995b, Crustal contamination in the petrogenesis of a calc-alkalic rock series: Josephine Mountain intrusion, California: Geological Society of America Bulletin, v. 107, p. 201–212. DOI: 10.1130/0016-7606(1995)107<0201:CCITPOO>>2.3.CO;2.

Barton, N., 2002, Some new Q-value correlations to assist in site characterisation and tunnel design. International Journal of Rock Mechanics and Mining Sciences., v. 39, p. 185–216, https://doi.org/10.1016/S1365-1609(02)00011-4.

Ben-Zion, Y., Peng, Z., Okaya, D., Seeber, L, Armbruster, J.G., Ozer, N.,. Michael, A.J., Baris, S., Aktar, M., 2003, A shallow fault-zone structure illuminated by trapped waves in the Karadere–Duzce branch of *the North Anatolian Fault, western Turkey, Geophysical Journal International,* v. 152, #3, p. 699–717, https://doi.org/10.1046/j.1365-246X.2003.01870.x.

Ben-Zion, Y., and Huang, Y., 2002, Dynamic rupture on an interface between a compliant fault zone layer and a stiffer surrounding solid, *Journal of Geophysical Research*, v..107(B2), doi:10.1029/2001JB000254.

Beyer, L.A., McCulloh, T.H., Denison, R.E., Morin, R.W., Enrico, R.J., Barron, J.A., and Fleck, R.J., 2009, Post-Miocene right separation on the San Gabriel and Vasquez Creek faults, with supporting chronostratigraphy, western San Gabriel Mountains, California: U.S. Geological Survey Professional Paper 1759, 27 p.

Bieniawski Z. T., 1978, Determining rock mass deformability: experience from case histories. Int J Rock Mechanics, Mining Sciences and Geomechanical Abstracts, v. 15, p.237–247.

_____1989, Engineering rock mass classifications. Wiley, New York, 250 p.

_____ 1993, Classification of rock masses for engineering: The RMR system and future trends, In: Hudson, J.A., ed., Comprehensive Rock Engineering, Volume 3: Oxford; New York, Pergamon Press, p. 553-573.

Blythe, A.E., House, M.A., and Spotila, J.A., 2002, Low-temperature thermochronology of the San Gabriel and San Bernardino Mountains, southern California: Constraining structural evolution, in Barth, A., ed., Contributions to Crustal Evolution of the Southwestern United States: Boulder, Colorado, Geological Society of America Special Paper 365, p. 231–250, doi:10.1130/0-8137-2365-5.231.

Boulton, C., Menzies, C.D., Toy, V.G., Townend, J. and Sutherland, R., 2017, Geochemical and microstructural evidence for interseismic changes in fault zone permeability and strength, Alpine Fault, New Zealand, Geochemistry, Geophysics, Geosystems, v.18, p. 238-265, https://doi.org/10.1002/2016GC006588.

Bradbury, K.K., Davis, C.R., Shervais, J.W., Janecke, S.U. and Evans, J.P., 2015, Composition, alteration, and texture of fault-related rocks from SAFOD core and surface outcrop analogs: Evidence for deformation processes and fluid-rock interactions. Pure and Applied Geophysics, v.172, p.1053-1078, DOI: https://doi.org/10.1007/s00024-014-0896-6.

Bruhn, R.L., Parry, W.T., Yonkee, W.A. and Thompson, T. (1994) Fracturing and Hydrothermal Alteration in Normal Fault Zones. Pure and Applied Geophysics, 142, 609-644. http://dx.doi.org/10.1007/BF00876057.

Bryant, W.A., compiler, 2017, Fault number 89c, San Gabriel fault zone, Newhall section, in Quaternary fault and fold database of the United States: U.S. Geological Survey, https://earthquakes.usgs.gov/hazards/qfaults.

Bull, W.B., 1978, South Front of the San Gabriel Mountains, southern California, Final Technical report, U.S. Geological Survey, https://hdl.handle.net/2027/uc1.31210012894836, 303 p.

Caine, J.S., Evans, J.P. and Forster, C.B., 1996, Fault zone architecture and permeability structure, Geology, v. 24, p.1025-1028, DOI:10.1130/0091-7613(1996)024<1025:FZAAPS>2.3.CO;2.

California High-Speed Rail Authority, 2019, Palmdale to Burbank Project Section, Preliminary Geotechnical Data Report for Tunnel Feasibility, Angeles National Forest, EEPB-KLF-TTK04-RE-0006_REV01 ANF PGDR, (https://hsr.ca.gov/high-speed-rail-in-california/project-sections/bakersfield-to-palmdale/), last accessed 4 October 2022.

Callahan, O.A., Eichhubl, P. and Davatzes, N.C., 2020, Mineral precipitation as a mechanism of fault core growth. Journal of Structural Geology, v.140, p.104-156, https://doi.org/10.1016/j.jsg.2020.104156.

Campbell, R. H., Wills, C. J., Irvine, P. J., Swanson, B. J., 2014, Preliminary Geologic Map of the Los Angeles 30’ x 60’ Quadrangle, California Version 2.0, California Geological Survey., scale1:10000.

Cardozo, N., and Allmendinger, R.W., 2013, Spherical projections with OSXStereonet: Computers & Geosciences, v. 51, p. 193 – 205, doi:10.1016/ j.cageo.2012.07.021.

Chester, F. M., and Chester, J. S.,1998, Ultracataclasite structure and friction processes of the Punchbowl fault, San Andreas system, California. Tectonophysics, v.295, p. 199-221, https://doi.org/10.1016/S0040-1951(98)00121-8.

Chester, F.M., J. P. Evans, and R. L Biegel, 1993, Internal structure and weakening mechanisms of the San Andreas fault. J. Geophysical Res., v. 98, p.771-786, 10.1016/S0040-1951(98)00121-8.

Chester, F. M., Logan, J. M. 1986, Implications for mechanical properties of brittle faults from observations of the Punchbowl fault zone, California, Pure and Applied Geophysics *v.* 124,p. 79-106, doi:10.1007/bf00875720.

D'Alessio, M.A., 2004, The Thermal and Mechanical Behavior of Faults, Ph.D. Dissertation, University of California, Berkeley, 162 p. https://seismo.berkeley.edu/Docs/d'Alessio_PhD_2004.pdf

Dibblee, T.W. Jr., 1991, Geologic Map of the Sundland and North ½ Burbank Quadrangles, Los Angeles, CA, Dibblee Geology Center, Map DF-32, scale 1:24000.

Dibblee, T.W. Jr., and Ehrenspeck, H.E., ed., 1991, Geologic map of the San Fernando and Van Nuys (north 1/2) quadrangles, Los Angeles County, California, Dibblee Geological Foundation, Dibblee Foundation Map DF-33, scale 1:24,000.

Dibblee, T.W. Jr., and Carter, B, 2002, Geologic Map of the Condor Peak Quadrangle, Los Angeles, CA, Dibblee Geological Foundation, Map DF-84, scale 1:24000.

Duan, Q., Yang, X., Ma, S., Chen, J. and Chen, J., 2016, Fluid–rock interactions in seismic faults: Implications from the structures and mineralogical and geochemical compositions of drilling cores from the rupture of the 2008 Wenchuan earthquake, China, Tectonophysics, v.666, p.260-280, DOI: https://doi.org/10.1016/j.tecto.2015.11.008.

Ehlig, P.L., 1973, History, seismicity and engineering geology of the San Gabriel fault, *in* Moran, D.E., Slosson, J.E., Stone, R.O., and Yelverton, C.A., eds., Geology, seismicity and environmental impact: Association of Engineering Geologist Special Publication, October 1973, p. 247–251.

Evans, J.P. and Chester, F.M., 1995, Fluid-rock interaction in faults of the San Andreas system: Inferences from San Gabriel fault rock geochemistry and microstructures, Journal of Geophysical Research: Solid Earth, v.100, p.13007-13020, DOI:10.1029/94JB02625.

Faulkner, D.R., Lewis, A.C., and Rutter, E.H., 2003, On the internal structure and mechanics of large strike-slip fault zones: Field observations of the Carboneras fault in southeastern Spain: Tectonophysics, v. 367, p. 235–251, doi:10.1016/S0040-1951(03)00134-3.

Faulkner, D. R., T. M. Mitchell, E. Jensen, and J. Cembrano, 2011, Scaling of fault damage zones with displacement and the implications for fault growth processes, Journal of Geophysical Research, v. 116, B05403, doi:10.1029/2010JB007788.

Ferrill, D.A., Morris, A.P., Evans, M.A., Burkhard, M., Groshong, R.H., and Onasch, C.M., 2004, Calcite twin morphology: A low-temperature deformation geothermometer: Journal of Structural Geology, v. 26, p. 1521–1529, doi:10.1016/j.jsg.2003.11.028.

Fialko, Y., Sandwell, D., Simons, M., and Rosen, P., 2005, Three-dimensional deformation caused by the Bam, Iran, earthquake and the origin of shallow slip deficit: Nature, v. 435, p. 295–299, doi:10.1038/nature03425.

Forand, D., Evans, J. P., Janecke, S. U., & Jacobs, J., 2017, Insights into fault processes and the geometry of the San Andreas fault system: Analysis of core from the deep drill hole at Cajon Pass, California. Geological Society of America Bulletin. https://doi.org/10.1130/B31681.1.

Gratier, J.-P., P. Favreau, and F. Renard, 2003, Modeling fluid transfer along California faults when integrating pressure solution crack sealing and compaction processes,, Journal of Geophysical Research., v. 108(B2), 2104, doi:10.1029/2001JB000380.

Hadizadeh, J., Mittempergher, S., Gratier, J.P., Renard, F., Di Toro, G., Richard, J. and Babaie, H.A., 2012, A microstructural study of fault rocks from the SAFOD: Implications for the deformation mechanisms and strength of the creeping segment of the San Andreas Fault, Journal of Structural Geology, v. 42, p.246-260, https://doi.org/10.1016/j.jsg.2012.04.011.

Haines, S.H., van der Pluijm,B. A. Ikari, M., Saffer, D., and Marone, C., 2009, Clay fabric intensity in natural and artificial fault gouges: Implications for brittle fault zone processes and sedimentary basin clay fabric evolution, Journal of Geophysical Research, v. 114, B05406,https://doi.org/10.1029/2008JB005866.

Hauksson, E. and Meier, M.A., 2019, Applying depth distribution of seismicity to determine thermo-mechanical properties of the seismogenic crust in southern California: comparing lithotectonic blocks, Pure and Applied Geophysics, v.176, p.1061-1081, https://doi.org/10.1007/s00024-018-1981-z.

Holdsworth, R. E., Van Diggelen, E. W. E., Spiers, C. J., De Bresser, J. H. P., Walker, R. J., & Bowen, L, 2011, Fault rocks from the SAFOD core samples: Implications for weakening at shallow depths along the San Andreas Fault, California. Journal of Structural Geology, v.33, p.132–144. https://doi.org/10.1016/j.jsg.2010.11.010.

Ishikawa, T., Tanimizu, M., Nagaishi, K., Matsuoka, J., Tadai, O., Sakaguchi, M., Hirono, T., Mishima, T., Tanikawa, W., Lin, W. and Kikuta, H., 2008; Coseismic fluid–rock interactions at high temperatures in the Chelungpu fault. Nature Geoscience, v. 1, p.679-683, https://doi.org/10.1038/ngeo308.

Ishikawa, T., Hirono, T., Matsuta, N., Kawamoto, K., Fujimoto, K., Kameda, J., Nishio, Y., Maekawa, Y., and Honda, G., 2014, Geochemical and mineralogical characteristics of fault gouge in the Median Tectonic Line, Japan: evidence for earthquake slip *Earth, Planets and Space* 66, 1-20, DOI:10.1186/1880-5981-66-36.

Jacobs, J. R., and Evans, J. P, and Kolesar, P. T., 2006, Chemical alteration in fault zones as sinks for “missing” earthquake energy, in: R. Abercrombie, H. Kanamori, and G. di Toro, eds., AGU Monograph 170, Earthquakes: Radiated Energy and the Physics of Faulting, p. 181-192, doii:10.1029/170GM18.

Jašarević, I., Kovćaević, M. S., 1996, Analyzing applicability of existing classification for hard carbonate rock in Mediterranean area. In: Proceedings of EUROCK’96, Turin, Italy, p. 811–818.

Jefferies, S.P., Holdsworth, R.E., Wibberley, C.A.J., Shimamoto, T., Spiers, C.J., Niemeijer, A.R., and Lloyd, G.E., 2006, The nature and importance of phyllonite development in crustal-scale fault cores: An example from the Median Tectonic Line: Japan: Journal of Structural Geology, v. 28, p. 220–235, doi:10.1016/j.jsg.2005.10.008.

Jennings, C.W., and Strand, R. G., 1969, Los Angeles Geologic Map, 1:250,000, California Division of Mines and Geology, Geologic Map of California.

Jeppson, T. N., Bradbury, K. K., and Evans, J. P. 2010, Geophysical properties within the San Andreas Fault Zone at the San Andreas Fault Observatory at Depth and their relationships to rock properties and fault zone structure, Journal of Geophysical Research, v. 115, B12423, doi:10.1029/2010JB007563.

Kaduri, M., Gratier, J.P., Renard, F., Çakir, Z. and Lasserre, C., 2017, The implications of fault zone transformation on aseismic creep: Example of the North Anatolian Fault, Turkey, Journal of Geophysical Research: Solid Earth, v. 122, p. 4208-4236, doi:10.1002/ 2016JB013803.

Kanamori, H., and Rivera, L., 2006, Energy partitioning during an earthquake: Geophysical Monograph Series. v. 170, p. 3–13, doi:10.1029/170GM03.

Kaneko, Y. and Fialko, Y., 2011, Shallow slip deficit due to large strike-slip earthquakes in dynamic rupture simulations with elasto-plastic off-fault response, Geophysical Journal International, v. 186, Pages 1389–1403, doi: 10.1111/j.1365-246X.2011.05117.x.

Marchandon, M., Hollingsworth, J. and Radiguet, M., 2021, Origin of the shallow slip deficit on a strike slip fault: Influence of elastic structure, topography, data coverage, and noise, Earth and Planetary Science Letters, v. 554, 11696, https://doi.org/10.1016/j.epsl.2020.116696.

Marone, C. and Saffer, D. M., 2007, Fault Friction and the Upper Transition From Seismic to Aseismic Faulting, in The Seismogenic Zone of Subduction Thrust Faults, Dixon, T. H. and Moore, J. C., eds., 692 p., Columbia University Press, DOI:10.7312/dixo13866-012.

Marone, C., and C. H. Scholz, 1988, The depth of seismic faulting and the upper transition from stable to unstable slip regimes, Geophysical Research Letters, v. 15, p. 621–624. doi:10.1029/GL015i006p00621.

Mavko, G., Mukerji, T., and Dvorkin, J., 2020, The Rock Physics Handbook, 3rd ed., Cambridge University Press, 756 p.

Miller, W. J., 1946, Crystalline rocks of southern California, Geological Society of America Bulletin, v. 57, p.457–542, doi:10.1130/0016-7606(1946)57[457:CROSC]2.0.CO:2.

Mitchell, T. M., & Faulkner, D. R. 2009. The nature and origin of off-fault damage surrounding strike-slip fault zones with a wide range of displacements: A field study from the Atacama fault system, northern Chile. Journal of Structural Geology, v. 31, p. 802–816. https://doi.org/10.1016/j.jsg.2009.05.002.

Mitri, H.S., Edrissi, R., Henning, J., 1994. Finite element modeling of cable bolted slopes in hard rock ground mines. In: Proceedings of the SME annual meeting, Albuquerque, New Mexico, February 1994, p. 94–116.

Nevitt, J.M., Brooks, B.A., Catchings, R.D., Goldman, M.R., Ericksen, T.L. and Glennie, C.L., 2020, Mechanics of near-field deformation during co-and post-seismic shallow fault slip, Scientific Reports, v.10, p.1-13, 10.1038/s41598-020-61400-9.

Nourse, J. A., 2002, Middle Miocene reconstruction of the central and eastern San Gabriel Mountains, southern California, with implications for evolution of the San Gabriel fault and Los Angeles basin, Geological Society of America Special Paper 365, p. 161–185, https://doi.org/10.1130/0-8137-2365-5.161.

Powell, R.E., 1993, Balanced palinspastic reconstruction of pre–late Cenozoic paleogeography, southern California, in Powell, R.E., et al., eds., The San Andreas fault system: Displacement, palinspastic reconstruction, and geologic evolution: Geological Society of America Memoir 178, p. 1–106, doi:10..1130/MEM178-P1.

Roten, D., Olsen, K. B., and Day, S. M., 2017, Off-fault deformations and shallow slip deficit from dynamic rupture simulations with fault zone plasticity, Geophysical Research Letters, v. 44, 15, https://doi.org/10.1002/2017GL074323.

Roten, D., Olsen, K. B., and Day, S. M., and Cui, Y., 2017, Quantification of fault-zone plasticity effects with spontaneous rupture simulations, Pure and Applied Geophysics, v. 174, p. 3369-3391, https://doi:10.1007/s00024-017-1466-6.

Rowe, C.D., Griffith, W.A., 2015. Do faults preserve a record of seismic slip: a second opinion. J. Struct. Geol.78, 1–26. https://doi.org/10.1016/j.jsg.2015.06.006.

Rowe, K. J. and Rutter, E.H., 1990, Palaeostress estimation using calcite twinning: experimental calibration and application to nature, Journal of Structural Geology, v. 12, p.1-17, https://doi.org/10.1016/0191-8141(90)90044-Y.

Schleicher, A.M., Tourscher, S.N., van der Pluijm, B.A. and Warr, L.N., 2009, Constraints on mineralization, fluid-rock interaction, and mass transfer during faulting at 2–3 km depth from the SAFOD drill hole, Journal of Geophysical Research: Solid Earth, v. 114, B04202, doi:10.1029/2008JB006092.

Schleicher, A.M., Van Der Pluijm, B.A. and Warr, L.N., 2012, Chlorite-smectite clay minerals and fault behavior: New evidence from the San Andreas Fault Observatory at Depth (SAFOD) core, Lithosphere, v.4, p.209-220, doi: 10.1130/L158.1.

Scholz, C. H., 1988, The brittle-plastic transition and the depth of seismic faulting. Geologische Rundschau, v.77,1, p.319-328, DOI:10.1007/BF01848693.

______, 2019, The Mechanics of Earthquakes and Faulting, 3rd edition, Cambridge University Press, 493 p.

Schulz, S.E., Evans, J.P., 1998, Spatial variability in microscopic deformation and composition of the Punchbowl fault, Southern California: implications for mechanisms, fluid-rock interaction, and fault morphology. Tectonophysics v. 295, p.223-244, https://doi.org/10.1016/S0040-1951(98)00122-X.

_____, 2000, Mesoscopic structure of the Punchbowl Fault, Southern California and the geologic and geophysical structure of active strike-slip faults, v. 22, p.. 913-930, https://DOI: 10.1016/S0191-8141(00)00019-5.

Serafim J. L., Pereira J. P., 1983, Considerations of the geomechanics classification of Bieniawski. In: Proceedings of the International Symposium on Engineering Geology and Underground Construction, Lisbon, Portugal, LNEC, Lisbon, 1983. p. 1. II-33–II-42.

Shinevar, W. J., Behn, M. D., Hirth, G., Jagoutz, O., 2018,Inferring crustal viscosity from seismic velocity: Application to the lower crust of Southern California, Earth and Planetary Science Letters, v. 494, p. 83-91, https://doi.org/10.1016/j.epsl.2018.04.055.

Sibson, R. H. 1977. Fault rocks and fault mechanisms. Journal of the Geological Society, London 133, 191–213, https://doi.org/10.1144/gsjgs.133.3.0191.

____1986, Earthquakes and rock deformation in crustal fault zones, Annual Review of Earth and Planetary Sciences, v.14, p.149-175 https://doi.org/10.1146/annurev.ea.14.050186.001053.

____, 2003, Thickness of the seismic slip zone, Bulletin of the Seismological Society of America, v.93, p.1169-1178. https://doi.org/10.1785/0120020061.

Simons, M., Fialko, Y. and Rivera, L., 2002, Coseismic deformation from the 1999 M w 7.1 Hector Mine, California, earthquake as inferred from InSAR and GPS observations, Bulletin of the Seismological Society of America, v.92, p.1390-1402. https://doi.org/10.1785/0120000933.

Singh, B. and Goel, R.K., 2011, Engineering rock mass classification), Elsevier, 364 p.

Studnicky, C., 2021, Constraining Deformation Mechanisms of Fault Damage Zones: A Case Study of the Shallow San Andreas Fault at Elizabeth Lake, Southern California. All Graduate Theses and Dissertations. 8134. https://digitalcommons.usu.edu/etd/8134.

Terzaghi, R. (1965) Sources of Error in Joint Surveys. Géotechnique, 15, 287-304. https://doi.org/10.1680/geot.1965.15.3.287.

Tokashiki N., Aydan O., 2012, Estimation of rock mass properties of Ryukyu limestone. In: Proceedings of the 7th Asian rock mechanics symposium, Seoul, Korea, p. 725–734.

Utada, M., 2001, Zeolites in burial diagenesis and low-grade metamorphic rocks: Reviews in Mineralogy and Geochemistry, v. 45, p. 276–304, doi:10.2138/rmg.2001.45.9.

Viesca, R. C.,. Templeton, E. L and Rice, J. R. 2008, Off-fault plasticity and earthquake rupture dynamics: 2. Effects of fluid saturation, Journal Geophysical Research, v,113, B09307, doi:10.1029/2007JB005530.

Warr, L.N. and Cox, S., 2001, Clay mineral transformations and weakening mechanisms along the Alpine Fault, New Zealand, Geological Society, London, Special Publications, v.186, p.85-101. https://doi.org/10.1144/GSL.SP.2001.186.01.06

Weber, F. H., Jr., 1982, Geology and geomorphology along the San Gabriel fault zone, Los Angeles and Ventura counties, California, California Division of Mines and Geology Open-File Report 82-02.

Wibberley, C.A.J. and Shimamoto, T., 2003, Internal structure and permeability of major strike-slip fault zones: the Median Tectonic Line in Mie Prefecture, Southwest Japan, Journal of Structural Geology v.25, p.59-78, doi:10:1016/S0191-8141(02)00014-7.

Wibberley, C.A.J., Yielding, G., and Di Toro, G., 2008, Recent advances in the understanding of fault zone internal structure; a review. In: Wibberley, C.A.J.,Kurz, W., Imber, J., Holdsworth, R.E., Collettini, C. (Eds.), Structure of Fault Zones: Implications for Mechanical and Fluid-flow Properties, Geological Society of London Special Publication, v. 299, p. 5-33, DOI: 10.1144/SP299.2 0305-8719/08.

Williams, C. F., and DeAngelo, J., 2011, Evaluation of Approaches and Associated Uncertainties in the Estimation of Temperatures in the Upper Crust of the Western United States, Geothermal Resource Council Transactions, v. 35, p. 1599-1605, https://publications.mygeoenergynow.org/grc/1029460.pdf.

Williams, R. T., Rowe, C. D., Okamoto, K., Savage, H. M., & Eves, E. 2021, How fault rocks form and evolve in the shallow San Andreas fault. *Geochemistry, Geophysics, Geosystems*, 22, e2021GC010092. https://doi.org/10.1029/2021GC010092.

Woodcock, N., and Mort, K., 2008, Classification of fault breccias and related fault rocks, Geological Magazine, v. 145, p. 435-550, https://doi.org/10.1017/S0016756808004883.

Yeats, R.S., Huftile, G.J., and Stitt, L.T., 1994, Late Cenozoic tectonics of the east Ventura basin, Transverse Ranges, California: American Association of Petroleum Geologists Bulletin, v. 78, p. 1040-1074, https://doi.org/10.32375/2001-GB77.12..

Yerkes, R. F., and Campbell, R. H., ., 2005, Preliminary Geologic Map of the Los Angeles 30' x 60' Quadrangle, Southern California, U. S. Geological Survey Open-file Report 2005-2019.

Zhang, L., 2016, Engineering Properties of Rocks, 2nd edition, Elsevier, 378 p.

Crouch et al Supplemental files

The supplemental files 1, 4, 5, 6, and 7 are stored at https://digitalcommons.usu.edu/all_datasets/193/, downloadable from Evans-20220502T171206Z-001.zip,. Supplemental files 2, 3, and 8 are downloadable from , The raw data files for the Palmdale to Burbank part of the California High-Speed Rail Authority (CHSRA) study were provided from open records request to CHSRA as part of the Draft Environmental Impact Study report (https://hsr.ca.gov/high-speed-rail-in-california/project-sections/bakersfield-to-palmdale/) via https://hsr-ca.nextrequest.com/. These files consist of parts of the entire report:

California High-Speed Rail Authority Palmdale to Burbank Project Section, Preliminary Geotechnical Data Report for Tunnel Feasibility, Angeles National Forest, and the related appendices:

Appendix A – Maps and Profiles

Appendix B – Report Figures

Appendix C – Drilling Summaries

Appendix D – Rock Core Borings

Appendix E – Petrography

Appendix F – Instrumentation

Appendix G – Geophysical Surveys

Appendix H – In-Situ Testing

Appendix I – Soil and Rock Laboratory Testing

Appendix J – Groundwater Laboratory Testing

Appendix K – Rock Mass Characterization

Appendix L – Geologic Structure Analysis

Supplemental Files

Supplemental File 1. Overview of the geometry and samples of the San Gabriel fault (SGF) sampled by the ALT-B2 drill core and the data collected from the drill core. Appendix A Data Overview at the data repository cited above includes:: Overview, Fault Geometry, Drill Core, Field Samples, Thin Sections, XRD, Geochemistry, and XRF Maps. The overview lists the drill core samples collected and the drill core box number they were collected from, the names of the thin sections and XRF maps associated with the drill core, and the names of the XRD and whole-rock geochemistry data associated with the drill core. The fault geometry lists the drill core and associated core box number, the upper and lower measured depths limits of the drill core samples in ALT-B2 (in meters), the measured distance of the samples from the main SGF along the measured depth of the ALT-B2 borehole, and the horizontal distance of the sample from the SGF trace. Descriptions of other sheets are detailed in the other appendices.

Supplemental File 2. Summary of core fracture data in the borehole. A. Summary of the nomenclature and criteria used in core logging, adapted from Kleinfelder report and Caltrans guidelines. Figure S2.2 and S2.3 show the data for fracture dips and fracture density data.
B. Table S2.1. Fracture dips and fracture density data as a function of depth. C. Fracture data from the Kleinfelder logs of core.

Supplemental File 3. Descriptions of field sites of the San Gabriel Fault. LT – Little Tujunga Canyon site, ~ 3.5 km from the drill site. BT- Big Tujunga Canyon site, 15-18 km south-southeast from the drill site.

Supplemental File 4. This file contains photos and descriptions of drill core from borehole ALT-B2. The file **ALT-B2 Core Photos** is a PDF with compiled images of bisected core, both dry and wet. Samples are oriented with measured depth along the borehole, with the upper and lower limits of the samples listed in meters and feet. Drill core samples were epoxied prior to their bisection. A complete list of samples, sample length (in both ft and m), measured depth along borehole ALT-B2, sample type, sample description notes, horizontal distance from the principal slip surface of the San Gabriel Fault, and year the sample was collected (in 2017 by C. Studnicky and 2019 by K. Crouch) is found in the excel spreadsheet **Appendix B_ALT-B2 Core Descriptions.** The total amount of drill core collected is calculated in meters and feet, and the amount of core in the subcategories of protolith, damage zone, and principal slip zone is listed (in m).

The associated folder **Core Pictures** contains the raw images of the epoxied and cut drill core samples with scale bars and color references. Images include both wet and dry samples. Photos and brief descriptions of drill core collected by C. Studnicky in 2017 are in PDF **Appendix B_DrillCorePhotos_2017.**

Supplemental File 5. Photos of outcrop samples from the Little Tujunga Canyon and Big Tujunga Canyon field sites. **Appendix C Field Sample Photos** contains compiled images of dry outcrop samples, with scale bar. Samples were collected by J. S. Caine in 1993 and prepared by J. P. Evans in 1994. Associated folder **Field Sample Photos** contains raw images of the outcrop samples.

Supplemental File 6. Descriptions and photomicrographs of thin sections from drill core from borehole ALT-B2 and outcrop samples from the Little and Big Tujunga Canyons. **Appendix D_Thin Sections** contains photomicrographs from drill core from borehole ALT-B2 and outcrop samples from the Little and Big Tujunga Canyons, in plane polarized and cross polarized light. Thin sections were scanned using an Epson Perfection Pro scanner. **Appendix D_ALT-B2 Thin Section Descriptions** contains thin section size, type, lithology, distance from the main trace of the San Gabriel fault (in m), and description notes of samples from the drill core. Thin sections from the Little and Big Tujunga Canyons were created in 1994 by J. P. Evans at USU.

Raw images of the thin sections are contained in the folder **Thin Section Scans**. Subfolders with that folder include ALT-B2 Thin Sections, Big Tujunga Thin Sections, and Little Tujunga Thin Sections. Image labels read as drill core number followed by .1, .2, etc. if there were multiple thin sections in one drill core samples.

Supplemental File 7. X-ray diffraction (XRD) data. **Appendix F_XRD Data** excel spreadsheet details sample name, sample measured depth along ALT-B2, sample type, and major, minor, and present minerals. Samples from core were analyzed at the USU Geosciences X-ray Diffraction Lab using the PANalytical X'Pert PRO XRD Spectrometer with monochromatic Cu K-α radiation. XRD data files are in folder **XRD Data.**

Supplemental File 8. Geotechnical data from the Draft Environmental Impact study for the CHSRA Palmdale to Burbank section of the rail line, and calculations for E, Vp, and Vs. Table S 8.1 – Raw data for core lithology, run hardness, weathering, fracture density, and rock mass rating parameters. RMR, and GSI. Results of calculations for Young's modulus of the rock mass, Poisson's ratio, and V_s and V_p values.

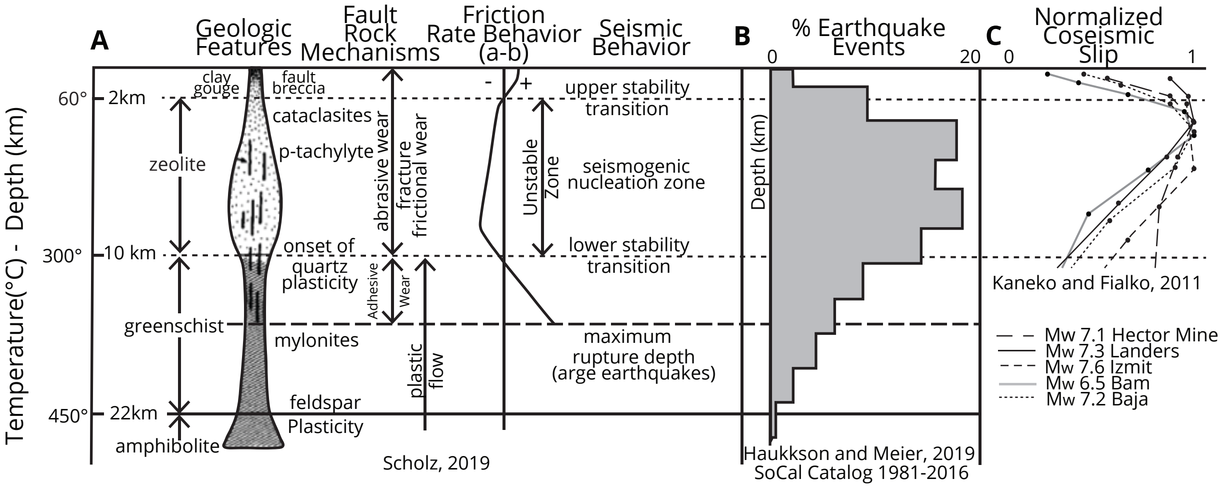

Crouch et al Figure 1

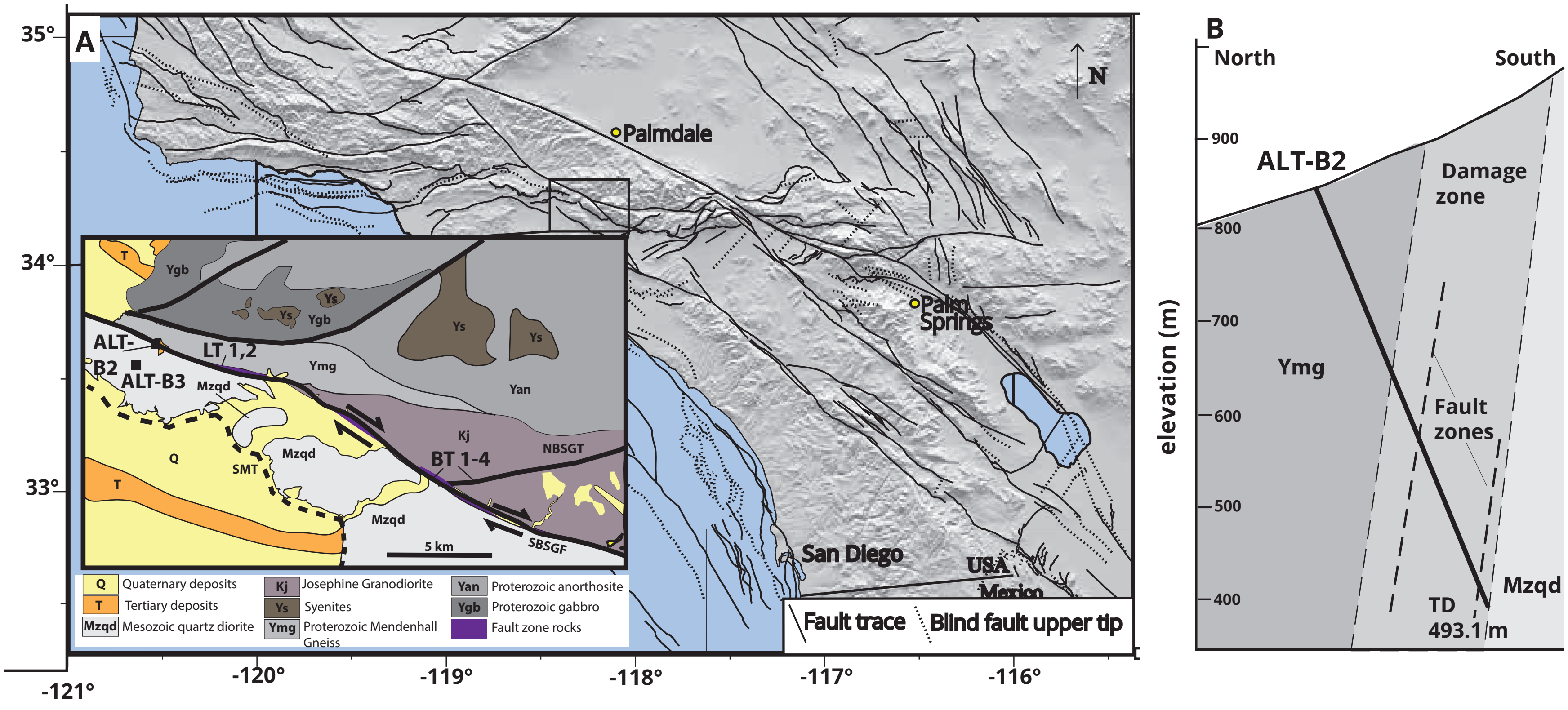

Crouch et al Figure 2

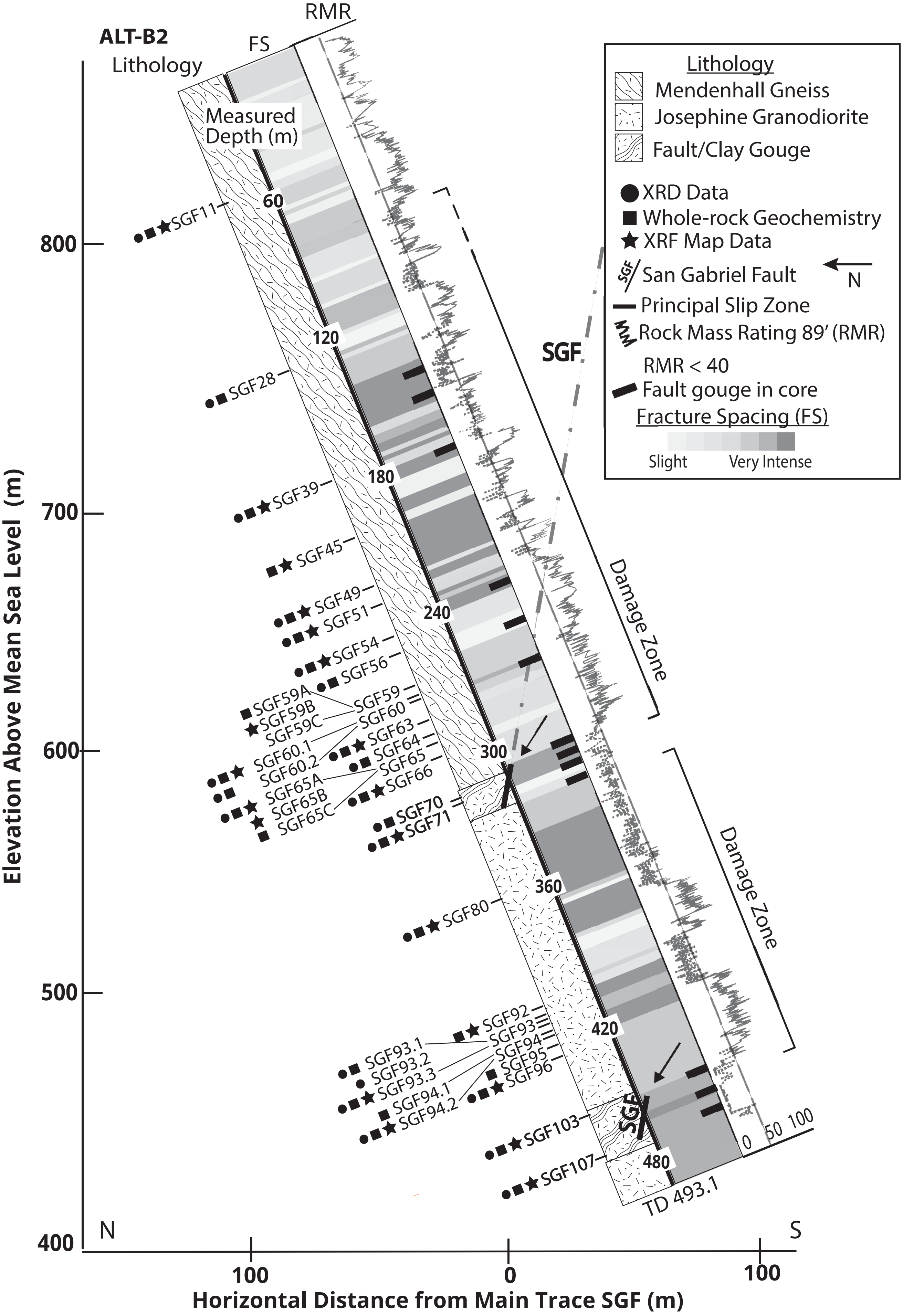

Crouch et al Figure 3

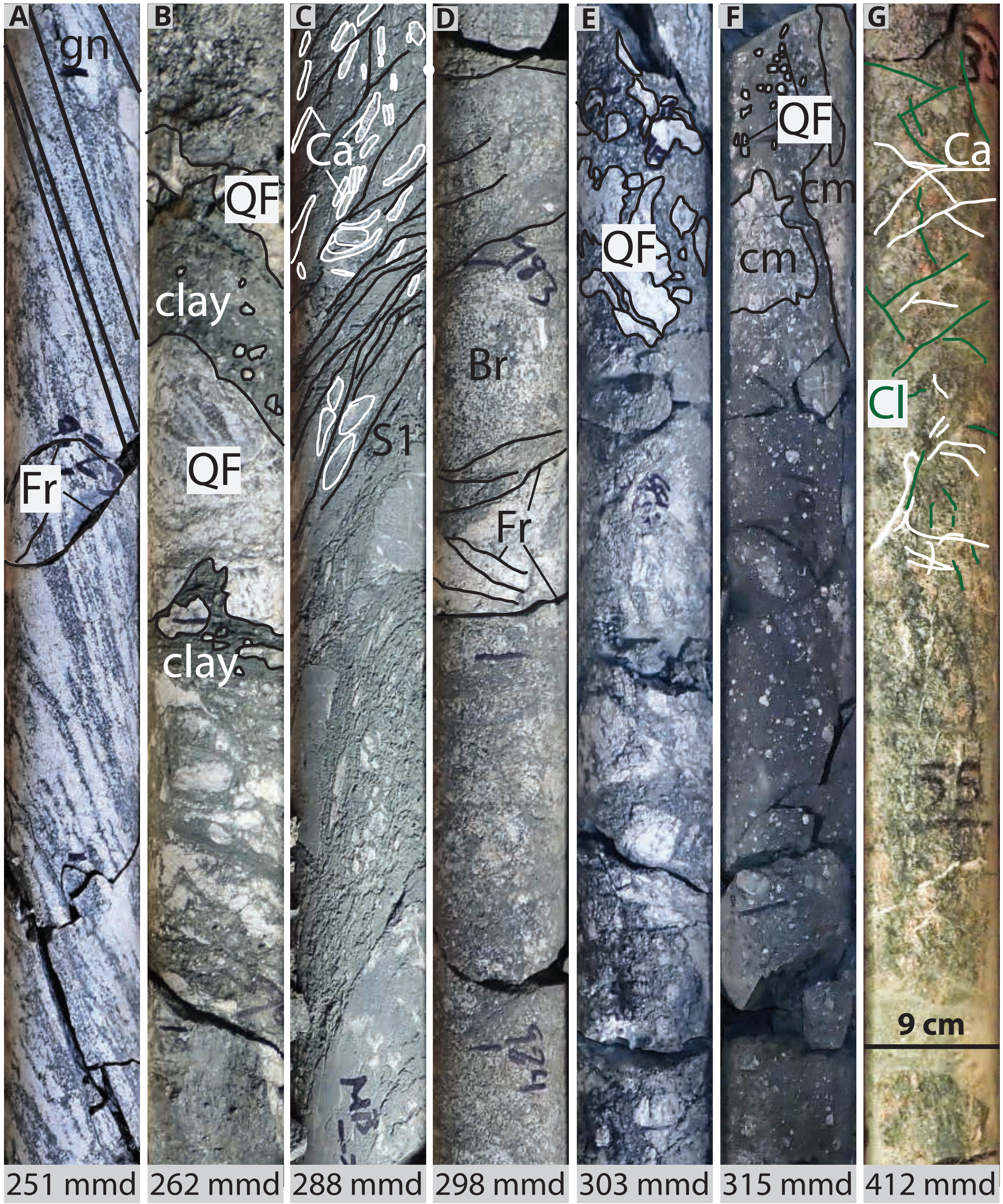

Crouch et al Figure 4

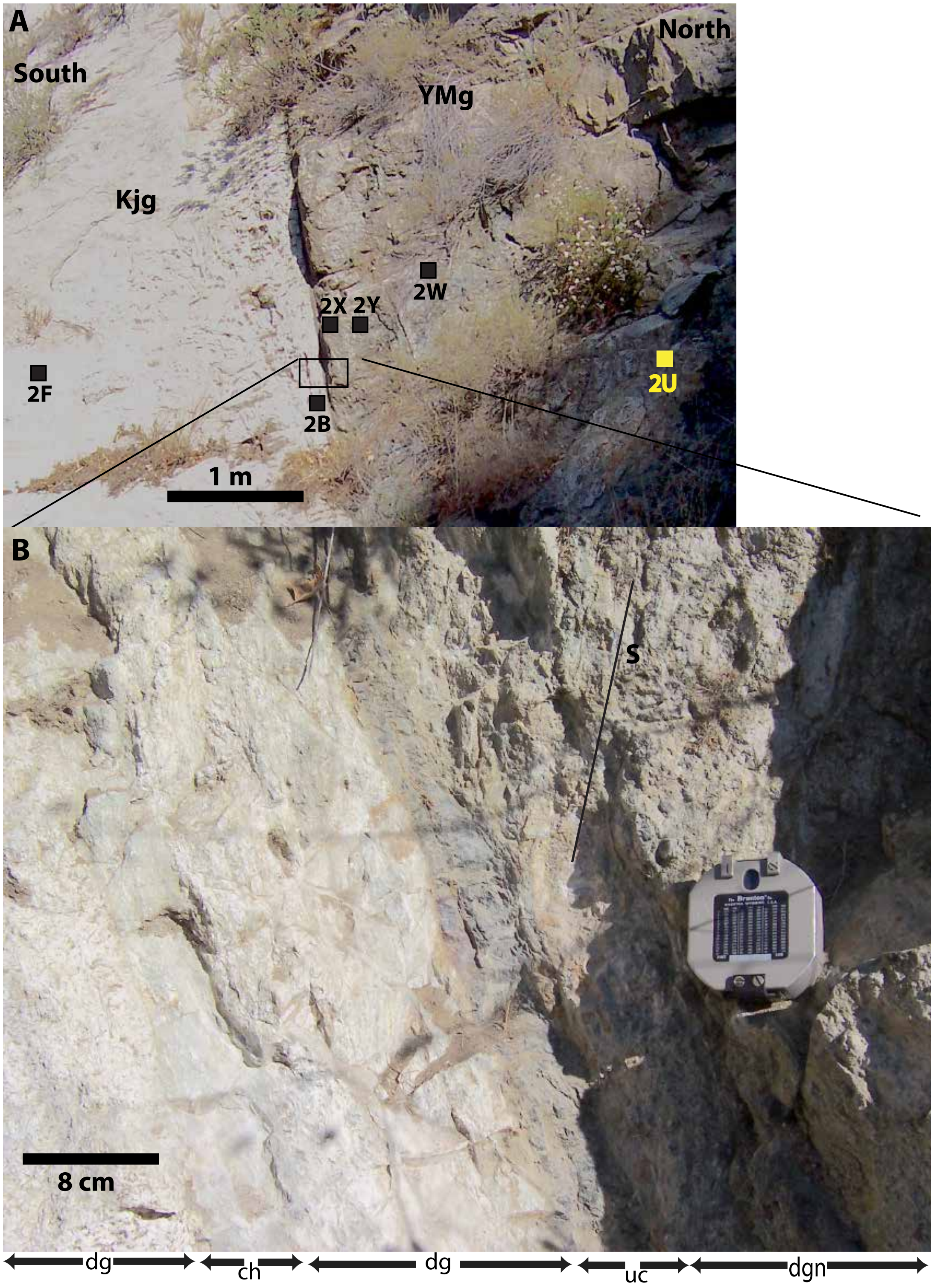

Crouch et al Figure 5

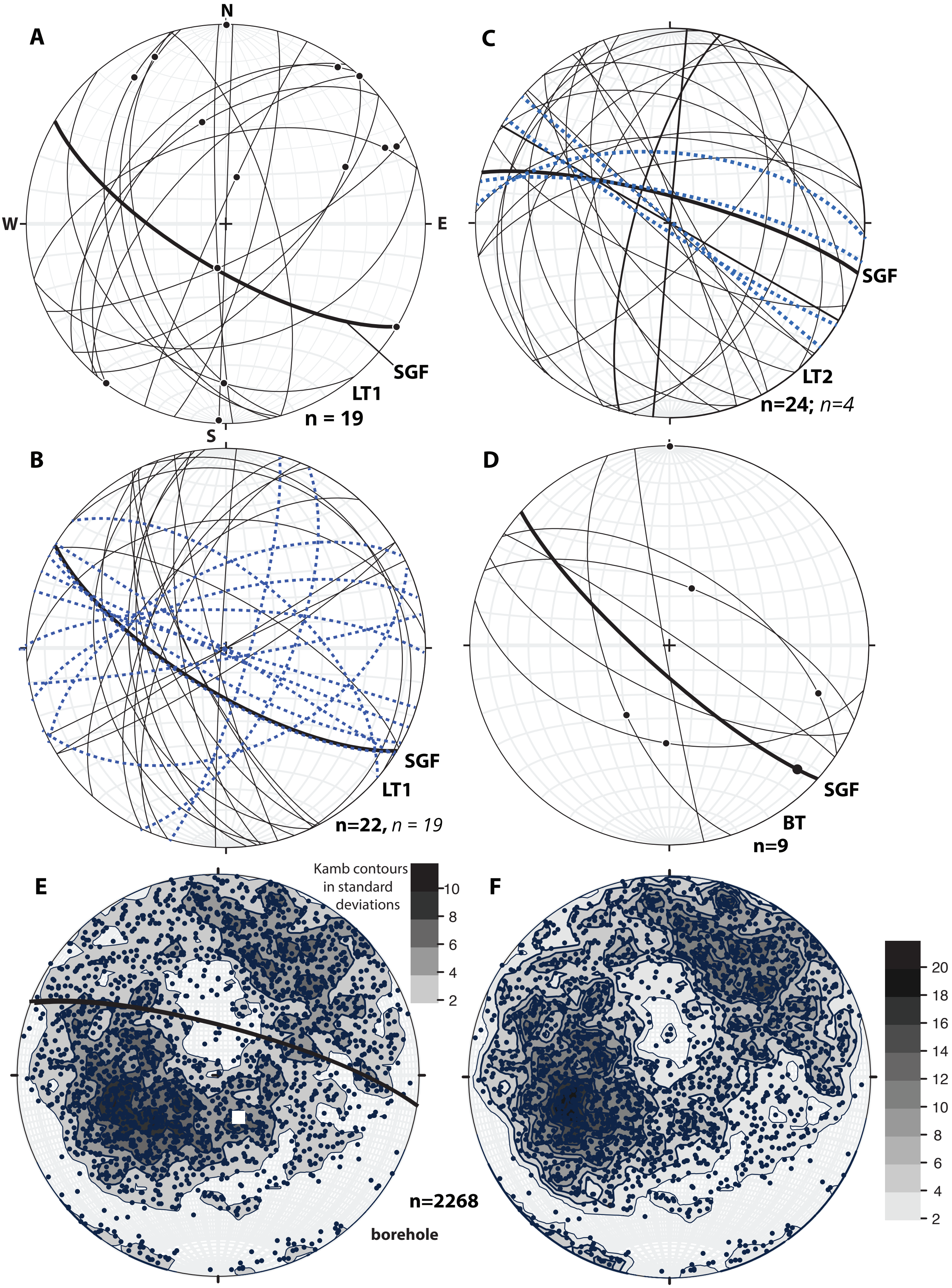

Crouch et al Figure 6

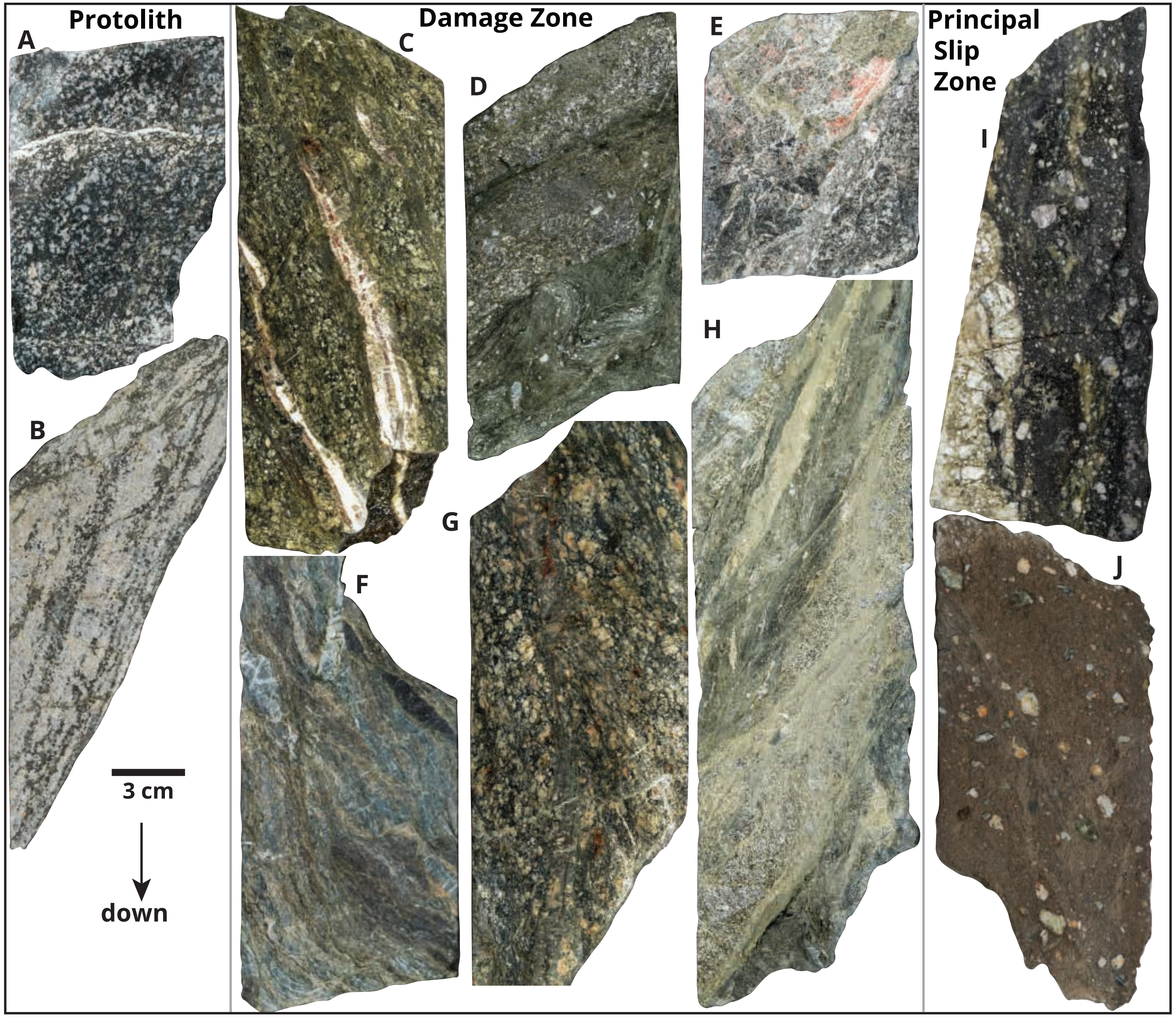

Crouch et al Figure 7

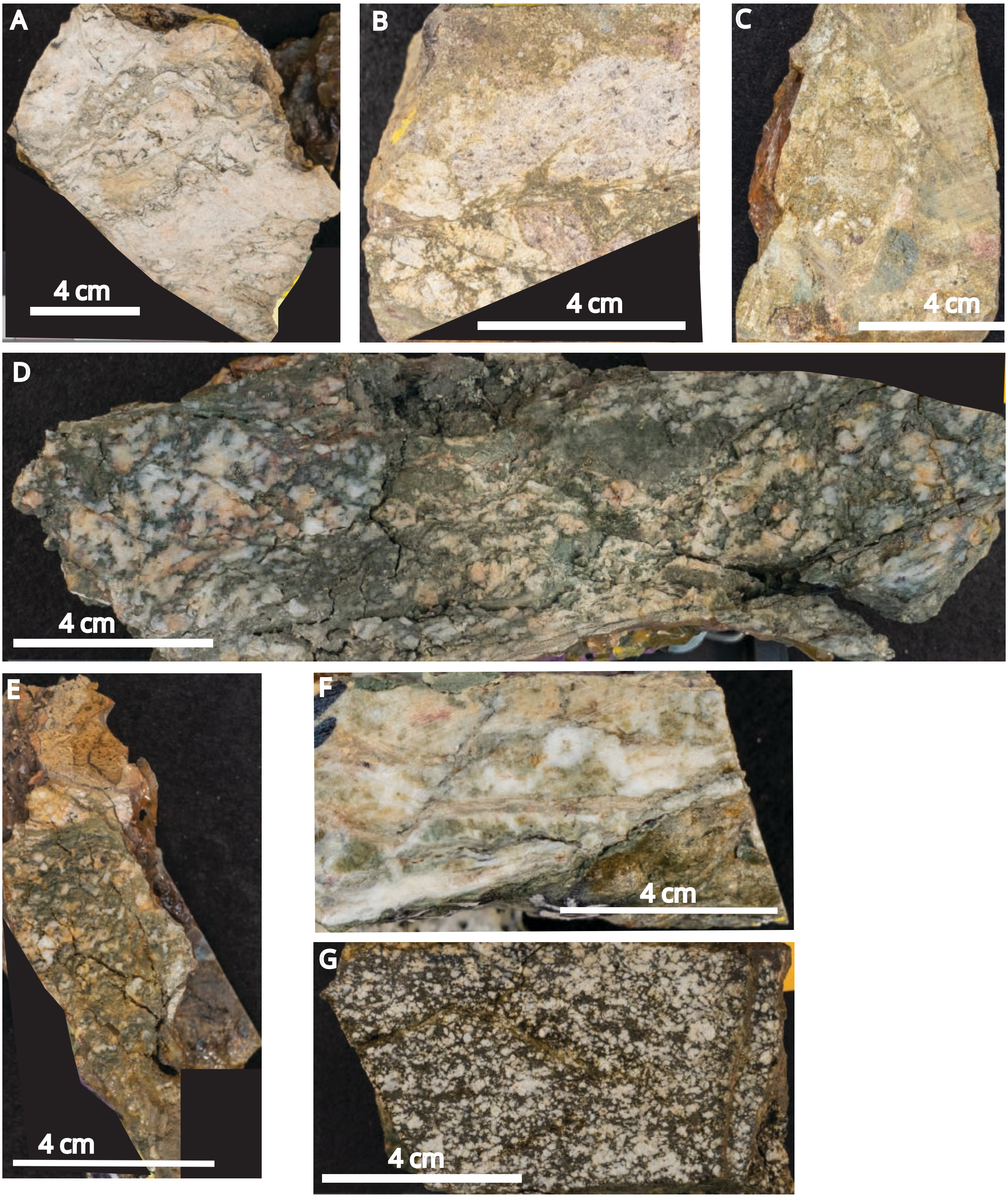

Crouch et al Figure 8

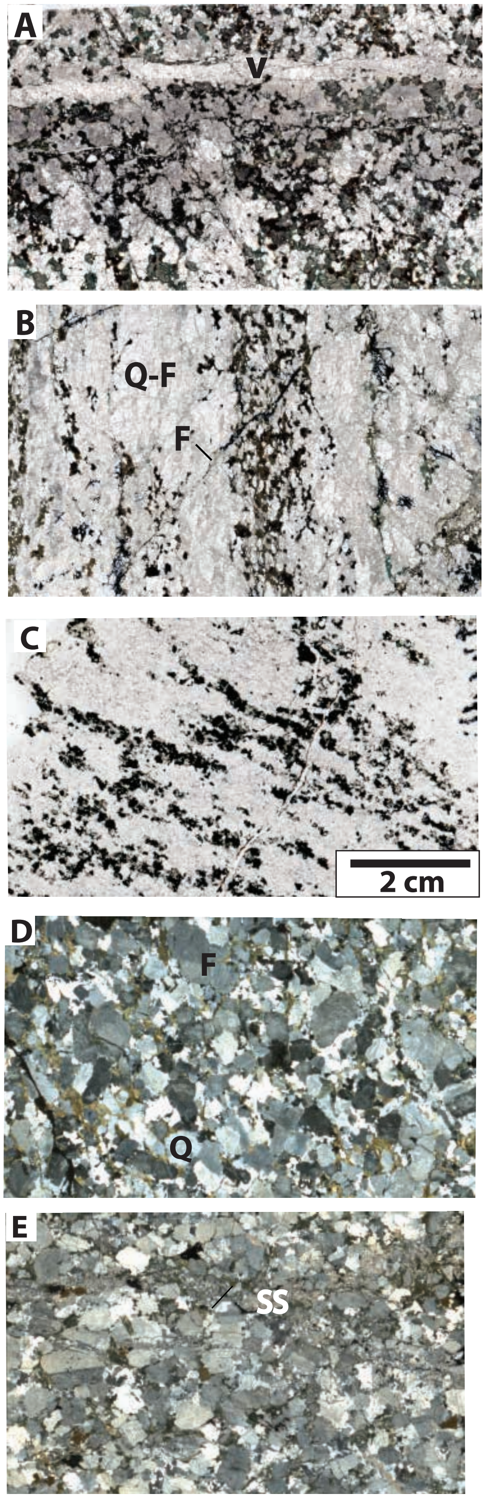

Crouch et al., figure 9

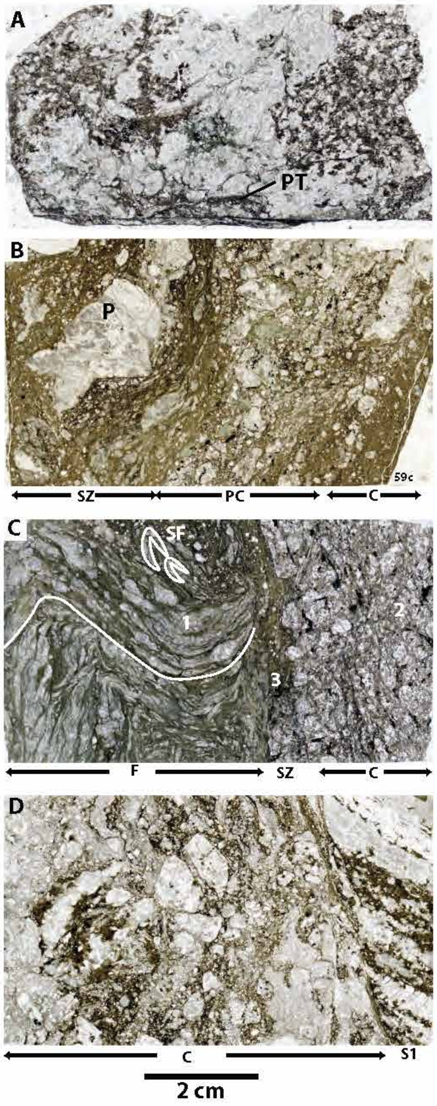

Crouch et al Figure 10

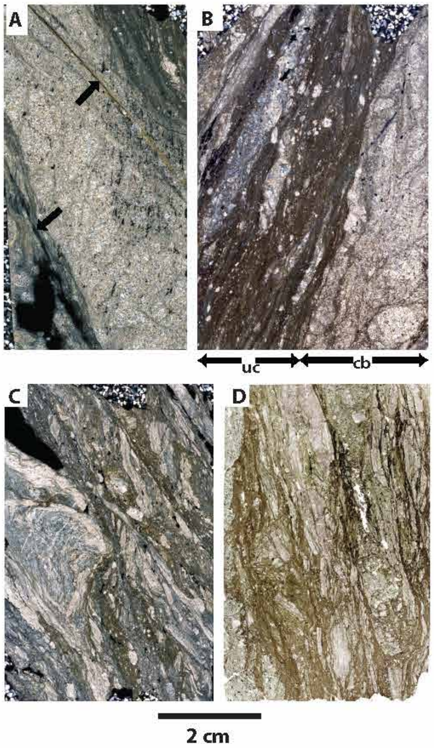

Crouch et al Figure 11

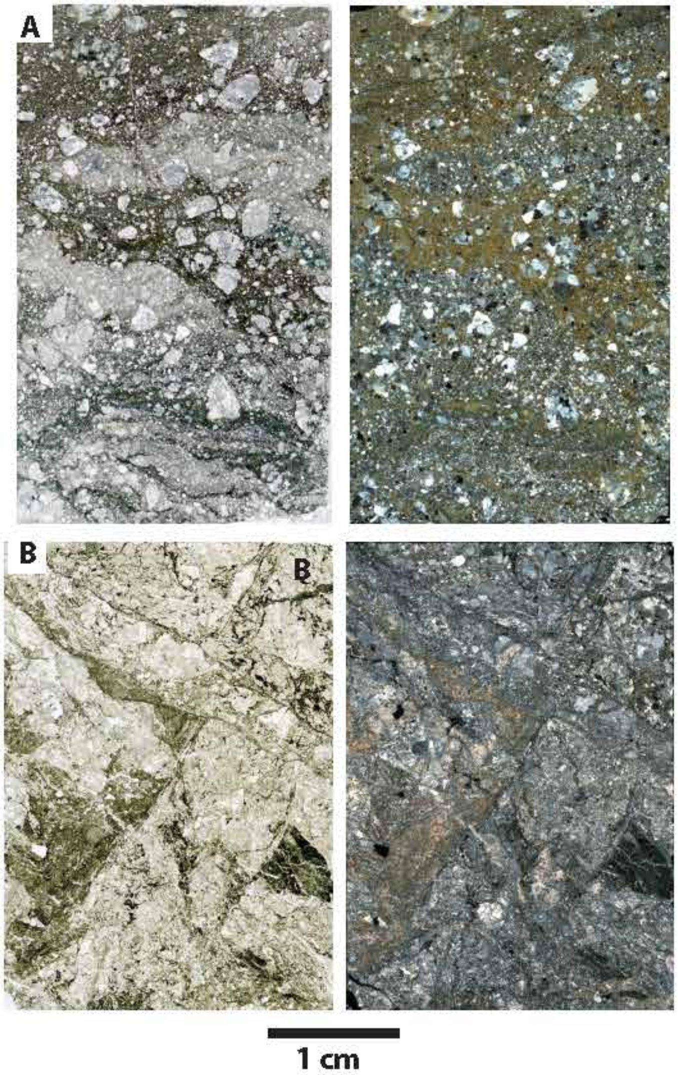

Crouch et al Figure 12

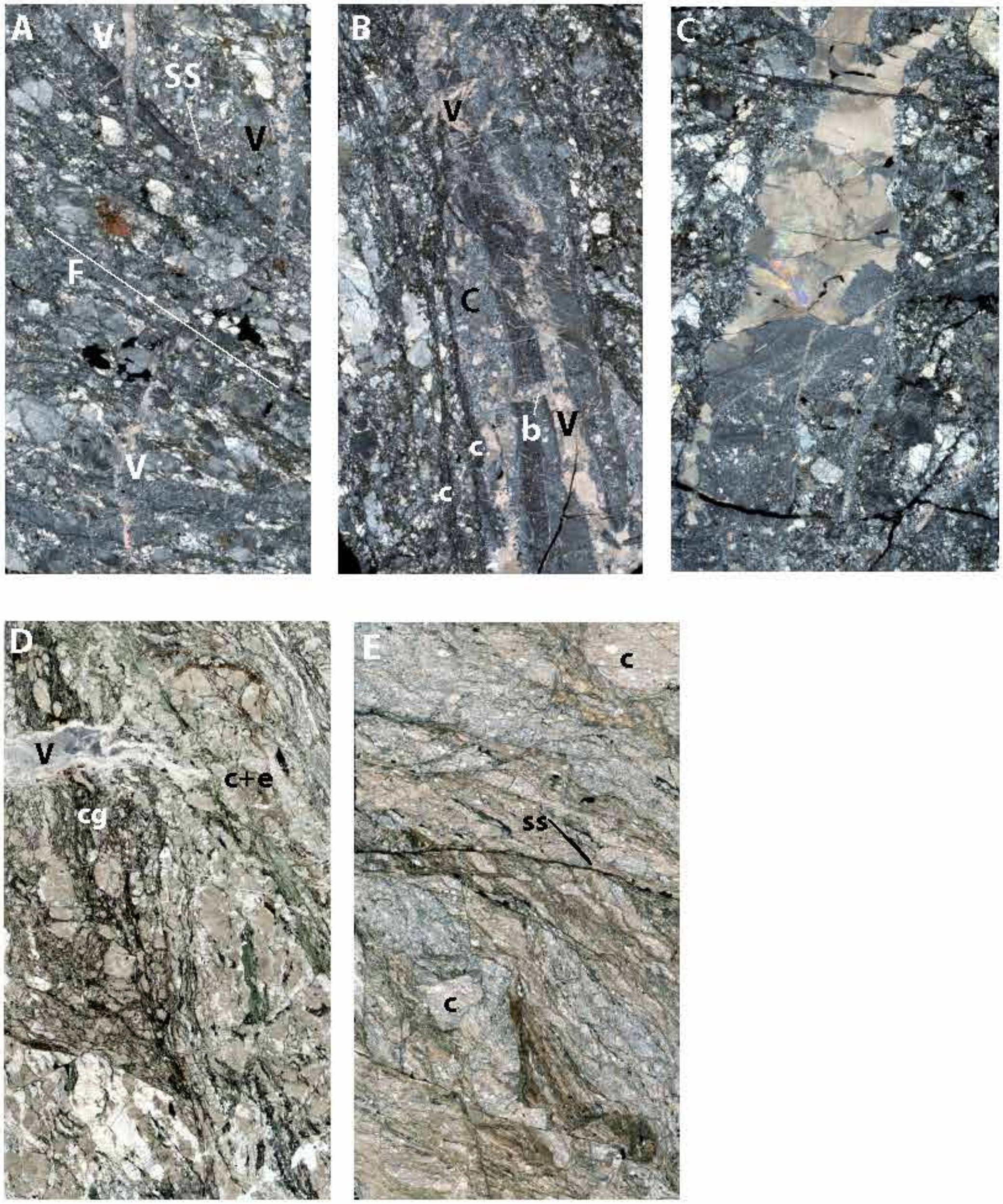

Crouch et al., Figure 13

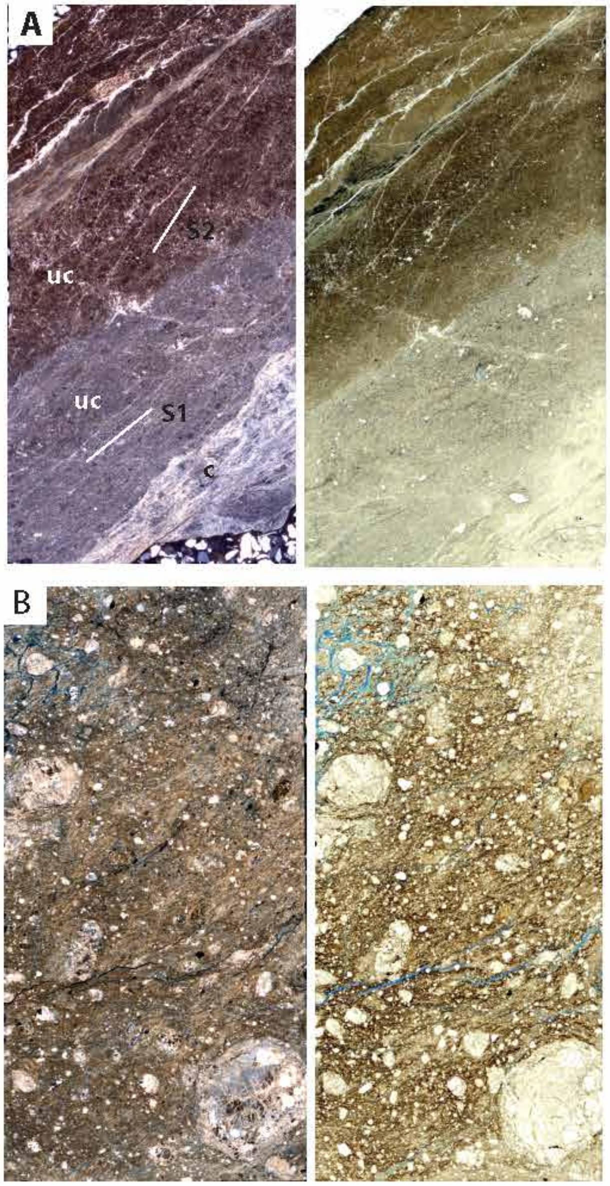

Crouch et al Figure 14

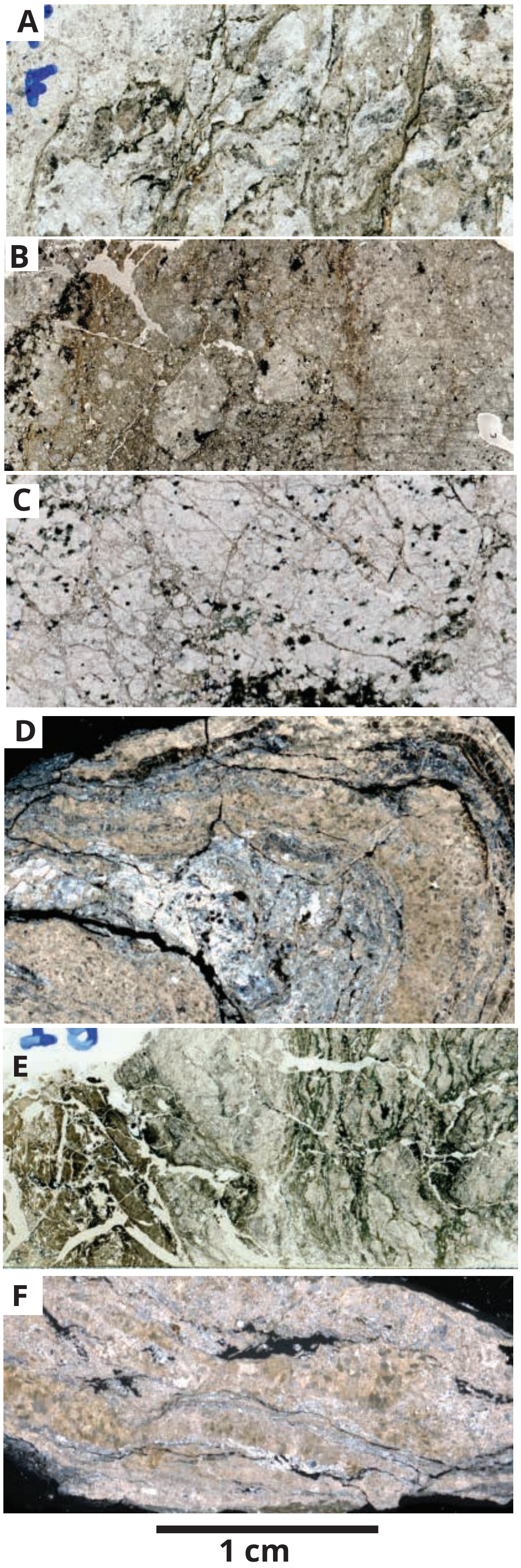

Crouch et aL Figure 15

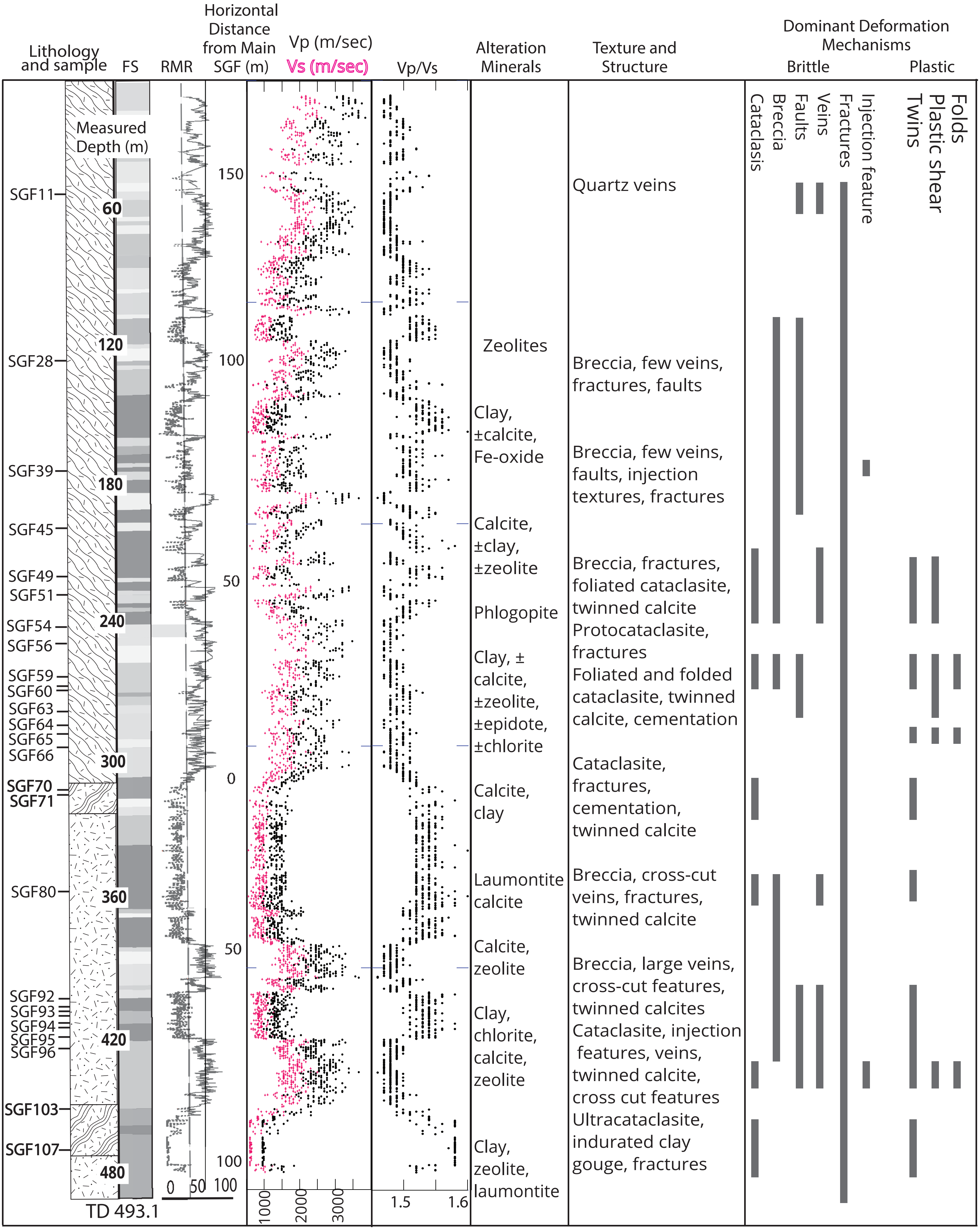

Crouch et al . Figure 16